P Wave Anisotropic Tomography of the SE Tibetan Plateau:Evidence for the Crustal and Upper-Mantle Deformations

doi: 10.1029/2018JB016048

Journal of Geophysical Research: Solid Earth

RESEARCH ARTICLE
10.1029/2018JB016048

P Wave Anisotropic Tomography of the SE Tibetan Plateau: Evidence for the Crustal and Upper-Mantle Deformations

Zhouchuan Huang[1,2], Liangshu Wang[1], Mingjie Xu[1], and Dapeng Zhao[3]

[1]Institute of Geophysics and Geodynamics, School of Earth Sciences and Engineering, Nanjing University, Nanjing, China, [2]Center of Modern Earth Sciences, Nanjing University, Nanjing, China, [3]Department of Geophysics, Tohoku University, Sendai, Japan

Key Points:
- We present a high-resolution *P* wave anisotropic tomography of the SE Tibetan Plateau
- Widespread low-velocity zones with margin-parallel anisotropy exist in the deep crust and uppermost mantle
- A shallow-crustal block drops down, causing deep-crustal and uppermost-mantle materials to extrude into adjacent regions

Supporting Information:
- Supporting Information S1
- Table S1
- Table S2

Correspondence to:
Z. Huang,
huangz@nju.edu.cn

Citation:
Huang, Z., Wang, L., Xu, M., & Zhao, D. (2018). *P* wave anisotropic tomography of the SE Tibetan Plateau: Evidence for the crustal and upper-mantle deformations. *Journal of Geophysical Research: Solid Earth*, *123*, 8957–8978. https://doi.org/10.1029/2018JB016048

Received 2 MAY 2018
Accepted 30 SEP 2018
Accepted article online 4 OCT 2018
Published online 29 OCT 2018

Abstract The upper crust in the SE Tibetan Plateau is rotating around the eastern Himalayan syntax clockwise, and the western margin of the Yangtze Craton has been involved in the active tectonics. However, it is still unclear whether and how the deep crust and upper mantle respond to the plateau expansion. In this study we present a high-resolution three-dimensional model of *P* wave velocity tomography and azimuthal anisotropy in the crust and uppermost mantle beneath the SE Tibetan Plateau determined using traveltime data recorded by a dense seismic network. Widespread low-velocity zones are revealed around a high-velocity body in the deep crust and uppermost mantle beneath the southwest Yangtze Craton, where fast-velocity directions of the azimuthal anisotropy are mostly parallel to the contour lines of the surface topography and the Moho depth along the plateau margin. These results indicate that gravitational potential plays an important role in the crustal and uppermost-mantle deformations in the SE Tibetan Plateau. Meanwhile, the shallow crust may drop down to the deep crust and drive the ductile deep-crustal material to intrude into the adjacent regions. The extruded crust is trapped in a deep-crustal corner and obstructed by the surrounding strong blocks. The trapped crustal material may rise up, causing significant uplift and high heat flow at the surface.

1. Introduction

The uplift of the Tibetan Plateau (Figure 1) is the most important geological process in East Asia in the Cenozoic (e.g., Li et al., 2015; Molnar & Tapponnier, 1975; Royden et al., 2008; Tapponnier et al., 2001; Yin, 2010). It results from the plate convergence between the Indian and Eurasian Plates in general. Many different mechanisms have been proposed to explain the rapid uplift. One kind of models suggests lithospheric deformation, for example, by the subduction or underthrusting of the Asian/Indian lithosphere beneath the plateau (e.g., Kind et al., 2002; Tapponnier et al., 2001; Zhao et al., 2010, 2011) or distributed shortening of the Asian lithosphere (e.g., England & Houseman, 1986; Zhang et al., 2004). Another kind of models emphasizes crustal deformations, by either distributed shortening (e.g., thrust faults; e.g., Zhang et al., 2004; Zuza et al., 2016) or lateral deep-crustal flow (e.g., Clark & Royden, 2000; Royden et al., 2008).

The SE Tibetan Plateau is a transition zone from high elevations (>3,000 m) in the plateau to low elevations (<1,000 m) in the South China and Indochina Blocks (Figure 1). The upper crust is rotating clockwise around the eastern Himalayan syntax (Figure 2a; Gan et al., 2007; Liang et al., 2013; Zheng et al., 2017), leading to strong sinistral shear along the Xianshuihe and Xiaojiang faults (Figure 2b; e.g., Kreemer et al., 2014; Pan & Shen, 2017). The deformation is also significant near the boundary between the Songpan-Ganzi Terrane and the South China Block, along the Lijiang-Xiaojinhe fault and the Muli and Jinhe-Qinghe thrust zones (Figures 1 and 2b; Ren, 1999; Wang et al., 2012). The South China Block is amalgamated by the Yangtze Craton and the Cathaysia Block in the Precambrian (Li et al., 2009). The Sichuan Basin, as the core of the Yangtze Craton, is a stable Archean block, which has little internal deformation (Wan, 2012). In contrast, the southwestern margin of the Yangtze Craton has been destructed, and petrological and geochemical researchers have suggested the existence of an Emenshan large igneous province covered by widespread Permian basalts in this area (Figure 1, inset; Ali et al., 2005; Xu et al., 2017). In the Cenozoic, the crustal extrusion accompanying the Tibetan Plateau uplift activated the southwestern cratonic margin, characterized by many active faults (e.g., the Xiaojiang, Anninghe, Zemuhe, and Daxianshan faults) and destructive earthquakes (Figures 1–3; e.g., Pan & Shen, 2017; Shen et al., 2005). Nevertheless, the active tectonics are limited to the Xiaojiang fault, whereas the Yangtze Craton to the east and the Youjiang Orogen

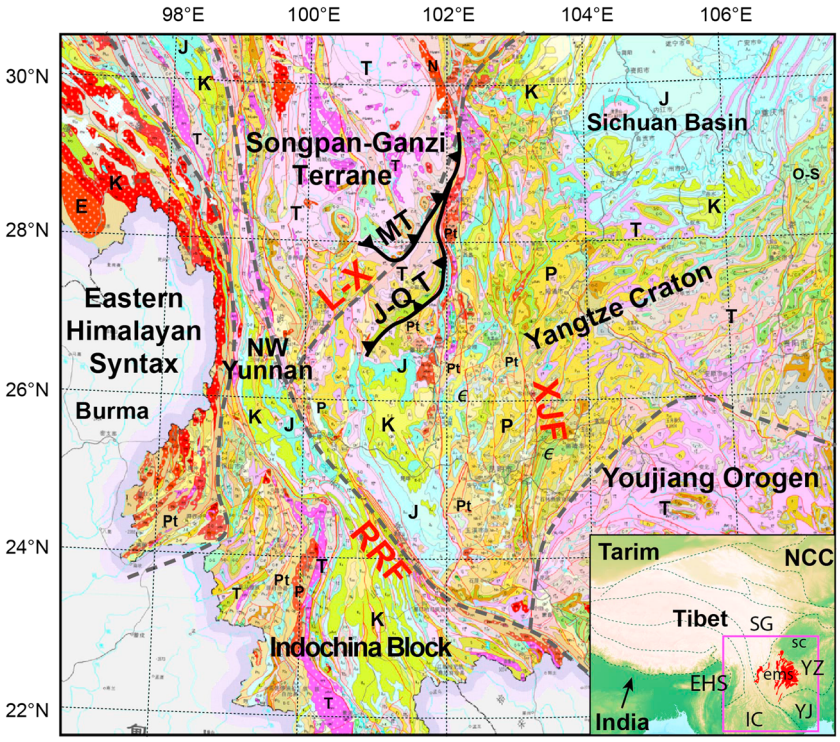

Figure 1. Geology of the SE Tibetan Plateau (China Geology Survey, 2002). The bold lines denote the Cenozoic thrust zones—Muli (MT) and Jinhe-Qinghe (J-Q T) thrust faults—along the boundary between the Songpan-Ganzi Terrane and the South China Block (e.g., the Yangtze Craton). The abbreviations are as follows: L-X = Lijiang-Xiaojinghe fault; XJF = Xiaojiang fault; RRF = Red River Fault. The periods of the sedimentary rocks are as follows: Pt = Precambrian; Є = Cambrian; O = Ordovician; S = Silurian; D = Devonian; C = Carboniferous; P = Permian; T = Triassic; J = Jurassic; K = Cretaceous; E = Paleogene; N = Neogene. The red and magenta regions with white crosses denote the igneous rocks. (inset) Tectonics in and around the Tibetan Plateau. Dashed lines denote major tectonic boundaries (Ren, 1999). The red colors denote the Permian volcanic rocks, named the Emenshan (ems) large igneous province (Ali et al., 2005; Xu et al., 2017). The abbreviations are as follows: SG = Songpan-Ganzi Terrane; EHS = eastern Himalayan syntax; YZ = Yangtze Craton; YJ = Youjiang Orogen; IC = Indochina Block; SC = Sichuan Basin.

(part of the Cathaysia Block) are less affected (Figure 2b). The shallow tectonics seem closely related to the deep-crustal structures, because the Moho is deeper than 45 km in the tectonically active regions (Figure 3).

Seismic anisotropy is an important feature of Earth materials (e.g., Babuska & Cara, 1991; Karato et al., 2008; Sun et al., 2016). It is generally caused by deformations in the Earth and so provides important information. Both the lattice preferred orientations of minerals (e.g., amphibole and mica in the mid-lower crust and olivine in the upper mantle) and shape preferred orientations of microstructures (e.g., cracks and melts) produce detectable seismic anisotropy (see Babuska & Cara, 1991; Karato et al., 2008; Ji et al., 2015; Silver, 1996; Weiss et al., 2014, for comprehensive reviews). The corresponding preferred orientation is generally parallel to the maximum-extension axis, that is, the maximum-shear direction for large shear strains (e.g., Karato et al., 2008). For typical channel flow in the deep crust, for example, under the Tibetan Plateau, the plastic flow can generally induce the flow-parallel fast orientations (Ko & Jung, 2015). When an *S* wave travels through the anisotropic media, it splits into two *S* waves with different velocities and perpendicular polarizations. Thus, shear-wave splitting (SWS) is sensitive to anisotropic media, making it a popular method to study anisotropy in the crust and upper mantle (e.g., Long & Silver, 2009; Silver & Chan, 1991). There have been many SWS measurements in the SE Tibetan Plateau using local *S* waves (e.g., Shi et al., 2012), Pms converted phases at the Moho (e.g., Cai et al., 2016; Chen et al., 2013; Sun et al., 2012), and teleseismic SKS/SKKS phases (e.g., Huang et al., 2007; Huang, Wang, et al., 2015; León Soto et al., 2012; Lev et al., 2006; Sol et al., 2007; Wang et al., 2008). While the SWS measurements provide important constraints on lateral variations of seismic anisotropy, they are unable to determine the depth of the anisotropic media. Hence, it is difficult to relate SWS measurements to crustal or upper-mantle deformations directly.

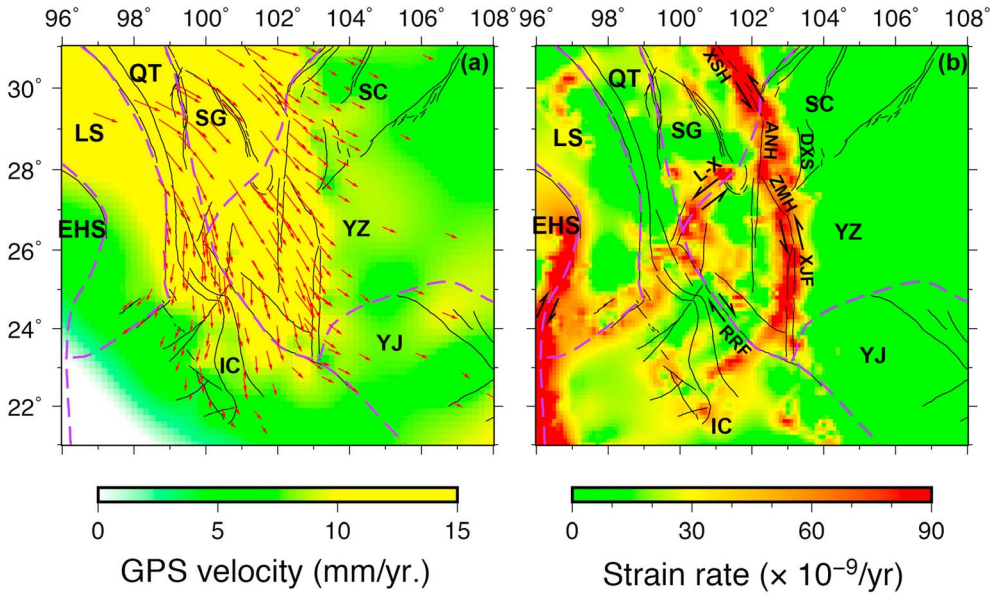

Figure 2. (a) Red arrows show the crustal motion revealed by the GPS observations relative to stable Eurasia (Gan et al., 2007; Pan & Shen, 2017). The background colors (and also the lengths of short bars) denote the horizontal GPS velocities. Dashed purple lines denote major tectonic boundaries (Ren, 1999). Black lines denote the active faults (Deng et al., 2003). (b) The strain rate in the SE Tibetan Plateau inverted from the GPS observations (Kreemer et al., 2014). See Figure 1 for the abbreviations; more abbreviations are as follows: LS = Lhasa Terrane; QT = Qiangtang Terrane; ANH = Anninghe fault; ZMH = Zemuhe fault; DXS = Daxianshan fault; GPS = global positioning system.

P wave anisotropic tomography is an important new method to determine three-dimensional (3-D) high-resolution seismic anisotropy in the crust and upper mantle (see Zhao et al., 2016, for a recent review). Applications of the method to subduction zones have revealed different features of anisotropy in the crust, mantle wedge, and subducting slabs (e.g., Eberhart-Phillips & Reyners, 2009; Huang et al., 2011; Liu & Zhao, 2016; Wang & Zhao, 2008), suggesting it is an effective method for studying the depth-dependent anisotropy. Its good vertical resolution complements the SWS analysis. In this study, we have picked a large number of *P* and *S* wave arrivals from seismograms of local earthquakes recorded by a dense seismograph network deployed in the SE Tibetan Plateau. Then we inverted the arrival time data for a high-resolution 3-D model of *P* wave velocity (Vp) tomography and azimuthal anisotropy. Our new data improve the resolution of Vp tomography in the lower crust and uppermost mantle significantly. The present results shed new light on crustal and upper-mantle deformations in the SE Tibetan margin.

2. Data and Method

2.1. Data

We first collected *P* and *S* wave arrival times generated by 221 earthquakes ($M \geq 3.0$) occurring in the SE Tibetan Plateau between August 2011 and August 2012 (Figure 4a). The earthquakes were recorded at a total of 557 stations that belong to two networks (Figure 4a). One network consists of 350 portable broadband stations (blue crosses in Figure 4a) deployed by the ChinArray project. We manually checked the seismograms (Figure 5) and picked 15,875 *P* and 11,179 S wave arrival times. For *P* waves, we usually picked the first arrivals, that is, direct waves (*Pg*) at short epicentral distances (e.g., $<$120 km) and head waves (*Pn*) and the waves traveling through the upper mantle at large distances (Figure 5a). The picking uncertainties are ~0.1 s. For *S* waves, however, the first arrivals are not clear at large distances. Hence, we picked the *S* wave arrivals with large amplitudes that in general correspond to the direct *S* waves (*Sg*; Figure 5b). The picking uncertainties could be 0.10 to 0.25 s. The other network consists of 207 permanent stations (blue squares in Figure 4a) belonging to the China Seismic Network (CSN) operated by the China Earthquake Administration. The China Earthquake Administration staff pick the arrival times manually and publish the phase reports online (http://data.earthquake.cn) for public access. We collected 4,665 *P* and 3,950 *S* wave arrival times of the

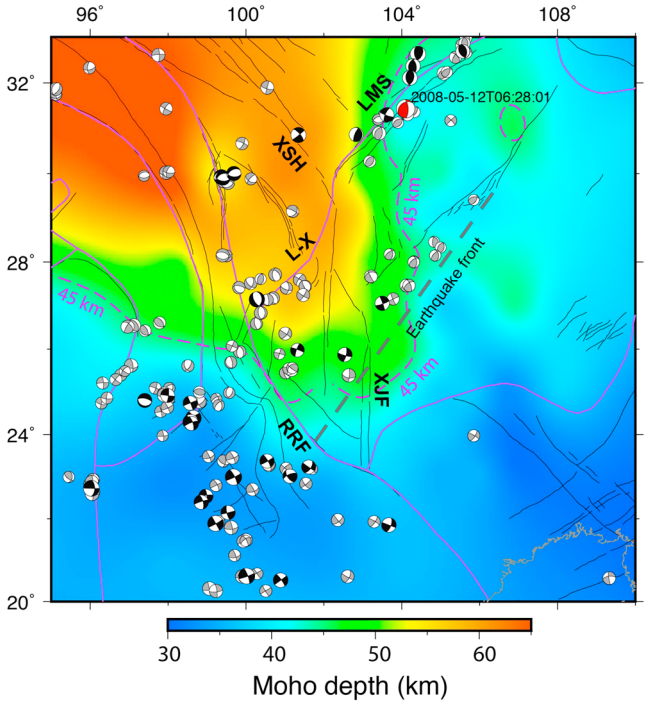

Figure 3. The Moho depth distribution in the SE Tibetan Plateau (Pasyanos et al., 2014; Wang et al., 2017). The dashed magenta lines denote the contour lines of the Moho depth at 45 km for later references. The beach balls show the focal mechanisms of earthquakes ($M \geq 5.5$) occurring between 1976 and 2017 (http://www.isc.ac.uk). The black balls show large earthquakes ($M \geq 6.0$). The red ball denotes the Wenchuan earthquake (M 7.9) that occurred on 12 May 2018. The white and shaded parts of each beach ball denote the tensional and compressional quadrants, respectively. The earthquake front (dashed line) marks the apparent boundary of the large earthquakes. Purple and black lines denote major tectonic boundaries (Ren, 1999) and the active faults (Deng et al., 2003), respectively. See Figure 1 for the abbreviations. LMS = Longmenshan fault.

221 earthquakes from the CSN reports. Thanks to the dense distribution of stations and large earthquake magnitudes ($M \geq 3.0$), we collected more than 160 arrival times for each event in average, including ~90 *P* and ~70 *S* wave arrivals in general. In addition, we also collected the arrival times of 1,552 events recorded only at the 207 CSN stations (Figure 4b). Every event has at least 15 records, and the minimal epicentral distance is smaller than 20 km, leading to precise hypocentral locations. These events generated 22,442 *P* wave and 19,009 S wave arrivals.

We constructed local *P* and *S* wave traveltime curves from the arrival-time data (Figure 5), and then determined the average one-dimensional (1-D) velocity model accordingly (Figure 6; e.g., Shearer, 2009). The average Vp and Vs are 6.00 and 3.52 km/s, respectively, in the upper crust, and are 7.85 and 4.47 km/s in the uppermost mantle right below the Moho. We estimated the velocities in the lower crust according to results from seismic exploration in this region (Zhang et al., 2011), because the earthquakes are mostly shallower than 20 km and so the traveltime curves for the *P*g and *S*g phases can only constrain the velocity in the upper crust. We set the Conrad discontinuity at 20-km depth following the global AK135 model (Kennett et al., 1995). The Moho geometry has been determined by receiver function analyses at 141 permanent and 785 temporary stations in southwest China (Wang et al., 2017), which is by far the best model for the Moho geometry in this region. Its lateral resolution is ~30 km according to the station density.

2.2. *P* Wave Anisotropic Tomography

P wave anisotropic tomography is an important expansion of traveltime seismic tomography, which can determine not only 3-D isotropic Vp distribution but also Vp azimuthal or radial anisotropy by inverting the traveltime data. It argues that Vp can be expressed as a function of the angle (θ) between the propagation direction and the hexagonal axis in a hexagonal medium (Calvet et al., 2006). The actual observations have proved that the anisotropic Vp (or slowness $S = 1/Vp$) variations are a function of the wave propagation azimuth (ϕ) in simple 2ϕ terms for weak azimuthal anisotropy (Raitt et al., 1969). For *P* wave rays with an incidence angle *i*, it is expressed as (Eberhart-Phillips & Henderson, 2004)

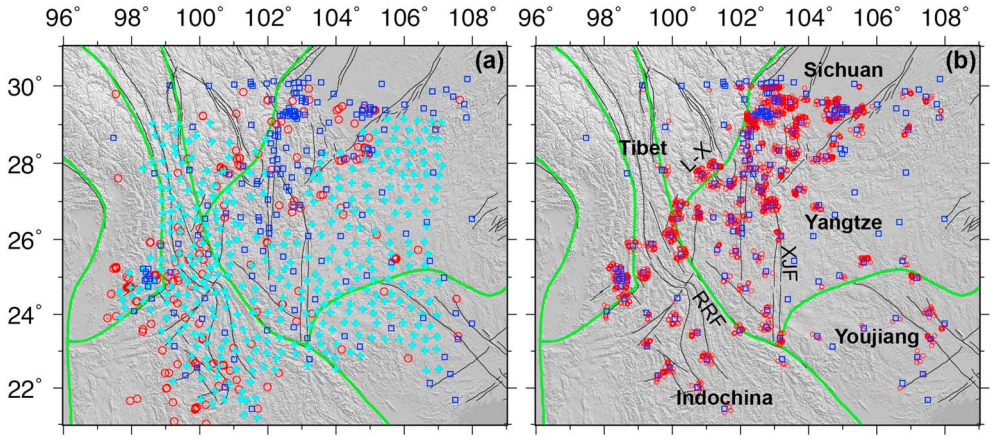

Figure 4. (a) Distribution of the 350 ChinArray stations (blue crosses) and 207 CSN stations (blue squares) and 221 local earthquakes (red circles) used in the study. (b) Epicentral distribution of 1,552 local events (red circles) recorded at the 207 CSN stations (blue squares). The minimal epicentral distances are smaller than 20 km. For the other labeling, see Figures 1 and 2. CSN = China Seismic Network.

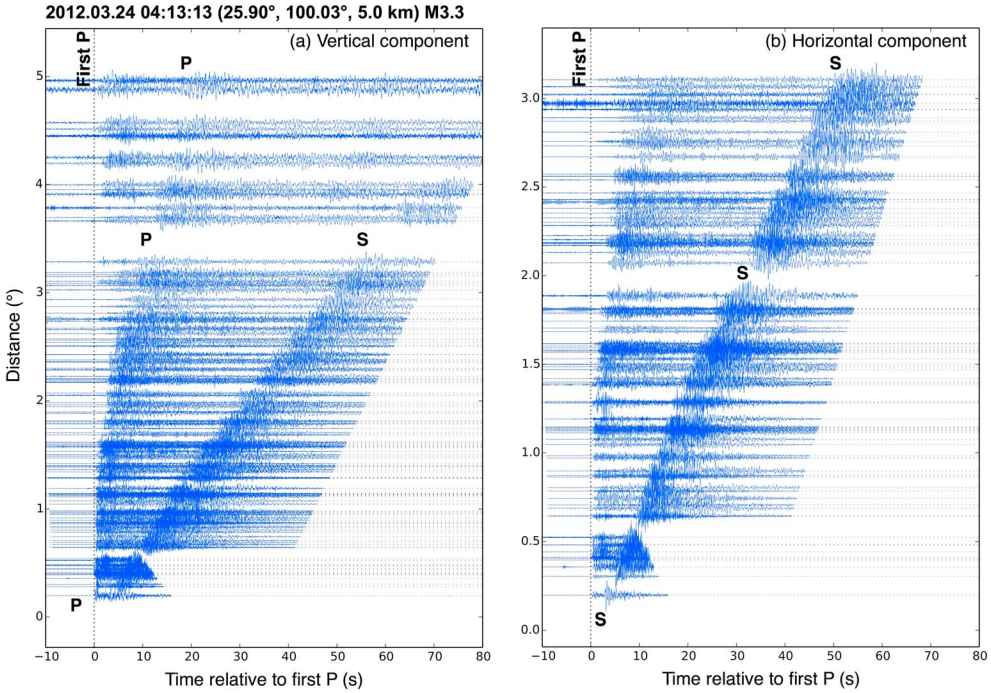

Figure 5. The seismic record sections for the (a) vertical and (b) horizontal components for a local earthquake (*M* 3.3). The seismograms are aligned by the synthetic first *P* wave arrivals calculated by using the Taup toolkit (Crotwell et al., 1999).

$$S(\phi) = S_0\left[1 - \cos^2 i\sqrt{A^2 + B^2} + \sin^2 i(A\cos 2\phi + B\sin 2\phi)\right] \tag{1}$$

where S_0 is the average isotropic slowness. The *P* wave azimuthal anisotropy is expressed as the strength of anisotropy (α):

$$\alpha(A,B) = \frac{\sqrt{A^2 + B^2}}{1 - \left(A^2 + B^2\right)} \times 100\% \tag{2}$$

and the fast-velocity direction (FVD, ψ):

$$\psi(A,B) = \begin{cases} \frac{1}{2}\cdot\tan^{-1}\left(\frac{B}{A}\right) + \begin{cases} \frac{\pi}{2}, A > 0 \\ 0, A < 0 \end{cases} \\ \left.\begin{cases} -\frac{\pi}{4}, B > 0 \\ \frac{\pi}{4}, B < 0 \end{cases}\right\}, A = 0 \end{cases} \tag{3}$$

The final observational equation for *P* wave azimuthal anisotropic tomography is

$$r = \frac{\partial T}{\partial \varphi_e}\cdot\Delta\varphi_e + \frac{\partial T}{\partial \lambda_e}\cdot\Delta\lambda_e + \frac{\partial T}{\partial h_e}\cdot\Delta h_e + \Delta T_e + \Sigma_{n=1}^{N}\left(\frac{\partial T}{\partial S_n}\cdot\Delta S_n\right) + \Sigma_{m=1}^{M}\left(\frac{\partial T}{\partial A_m}\cdot\Delta A_m + \frac{\partial T}{\partial B_m}\cdot\Delta B_m\right) \tag{4}$$

where r is the observed traveltime residuals, ($\Delta\varphi_e$, $\Delta\lambda_e$, Δh_e) and ΔT_e are perturbations of the hypocentral location and origin time, respectively, and ΔS is the isotropic slowness (velocity) perturbations relative to the 1-D model. The partial derivatives of the traveltime with respect to the hypocentral parameters ($\partial T/\partial\varphi_e$, $\partial T/\partial\lambda_e$, $\partial T/\partial h_e$) and the slowness at each grid node ($\partial T/\partial S_n$) can be calculated straightforwardly (Engdahl & Lee, 1976). The previous terms define traditional traveltime tomography for the isotropic velocity anomalies. The remaining terms, that is, perturbations of the anisotropic parameters A and B (ΔA, ΔB) and the

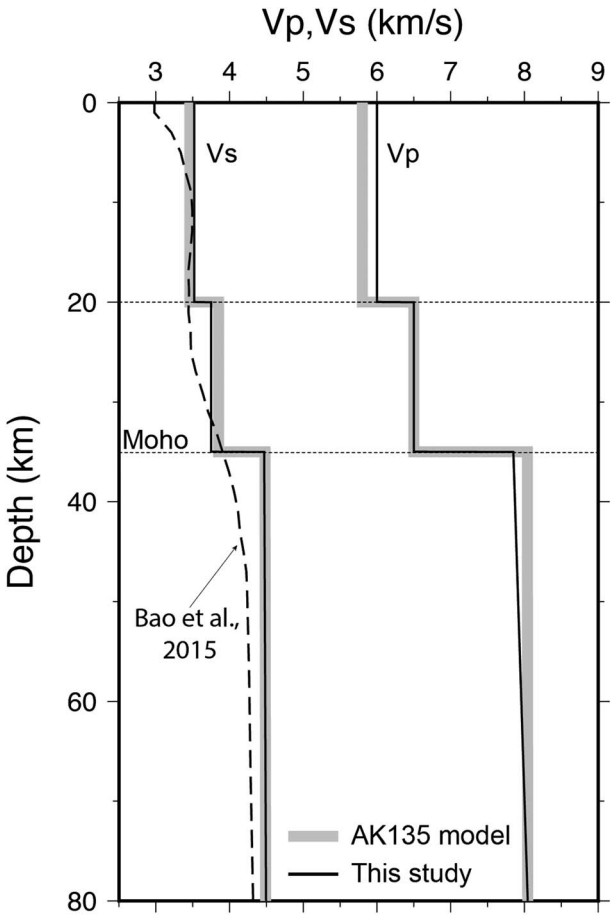

Figure 6. The 1-D *P* and *S* wave velocity models used in the study (black lines) as well as the global AK135 model (bold gray lines; Kennett et al., 1995) for reference. The dashed line shows the average 1-D *S* wave velocity derived from the joint inversion of surface wave and receiver functions (Bao et al., 2015).

corresponding partial derivatives ($\partial T/\partial A_m$, $\partial T/\partial B_m$) represent *P* wave azimuthal anisotropy (see Eberhart-Phillips & Henderson, 2004; Eberhart-Phillips & Reyners, 2009; Wang & Zhao, 2008, for details).

We assumed that the hexagonal symmetry has a horizontal orientation in the *P* wave anisotropy tomography. However, inclined hexagonal symmetry is common, particularly beneath continents (due to fossil anisotropy in complex folds; e.g., Babuška et al., 1993; Plomerová & Babuška, 2010) and subduction zones (due to 3-D mantle flow; e.g., Wang and Zhao, 2013; Huang, Zhao, et al., 2015). In this study, in order to reduce the influence of inclined symmetry, we only used subhorizontal ray segments ($60° < i < 120°$, i.e., within 30° angle from horizontal) to constrain the *P* wave azimuthal anisotropy.

2.3. Tomographic Inversion

We inverted the arrival-time data for 3-D isotropic Vp and its azimuthal anisotropy simultaneously (e.g., Wang & Zhao, 2008; Zhao et al., 1992) by solving the observational equations (equation (4)). Two grid nets with a lateral grid interval of ~50 km at 10-, 25-, 40-, and 60-km depths are arranged in the study volume to express the 3-D isotropic Vp and its azimuthal anisotropy separately. The perturbations of the isotropic Vp (or slowness, ΔS) and the anisotropy parameters (ΔA, ΔB) at any point are calculated by linearly interpolating the perturbations at the eight adjacent grid nodes of the corresponding grid net. We used a 3-D ray tracing technique (Zhao et al., 1992) that combines the pseudo-bending algorithm (Um & Thurber, 1987) and Snell's law to compute theoretical traveltimes and ray paths, which also incorporates station elevations and an undulating Moho discontinuity. We applied the LSQR algorithm (Paige & Saunders, 1982) to solve the observational equations (equation (4)) with proper smoothing and damping regularizations (Lees & Crosson, 1989) based on the trade-off curve between the traveltime residuals and the model norms. We conducted the tomographic inversion three times iteratively. The earthquakes are all relocated with the newly determined 3-D Vp models during the iterations.

3. Results

3.1. Checkerboard Resolution Test

Figure 7 shows the distribution of ray paths from the events to the stations used in this study. Although we used more arrivals recorded at the CSN stations, the corresponding ray paths only cover an NE–SW belt along the Tibet-Yangtze boundary in the crust (Figure 7b). The ray coverages in the adjacent regions and especially at 50- to 80-km depths are very poor, because the arrivals were picked only at short epicentral distances for locating local earthquakes. The new data we picked greatly improve the ray coverage, for example, within the plateau and craton (Figure 7a). More importantly, we picked many first *P* wave arrivals at long distances, thanks to the many stations and large earthquake magnitudes ($M \geq 3.0$). The seismic rays at long distances travel in the deep crust and upper mantle, improving the ray coverage there significantly.

Figure 8 shows the accumulated weight (calculated by linearly interpolating) at every grid node, providing an average relative measure of the density of seismic rays. It is sensitive to the spatial separation of a ray from the nodal location and so better reflects the seismic ray distribution than an unweighted count of the total number of rays around a node (e.g., Toomey & Foulger, 1989). In most parts of the study region, the accumulated weights at the grid nodes are larger than 100 (Figure 8), suggesting good ray coverage. The ray coverage is relatively poor at 25-km depth where the accumulated weights are smaller than 100. We also show ray ellipses that approximately represent the ray-azimuthal coverage (Huang, Zhao, et al., 2015). The short-to-long axis ratio of the ray ellipse equals to 1 when the rays are evenly distributed in all azimuths, and approaches 0 when all the rays are confined to a narrow range of azimuth (see Huang, Zhao, et al., 2015,

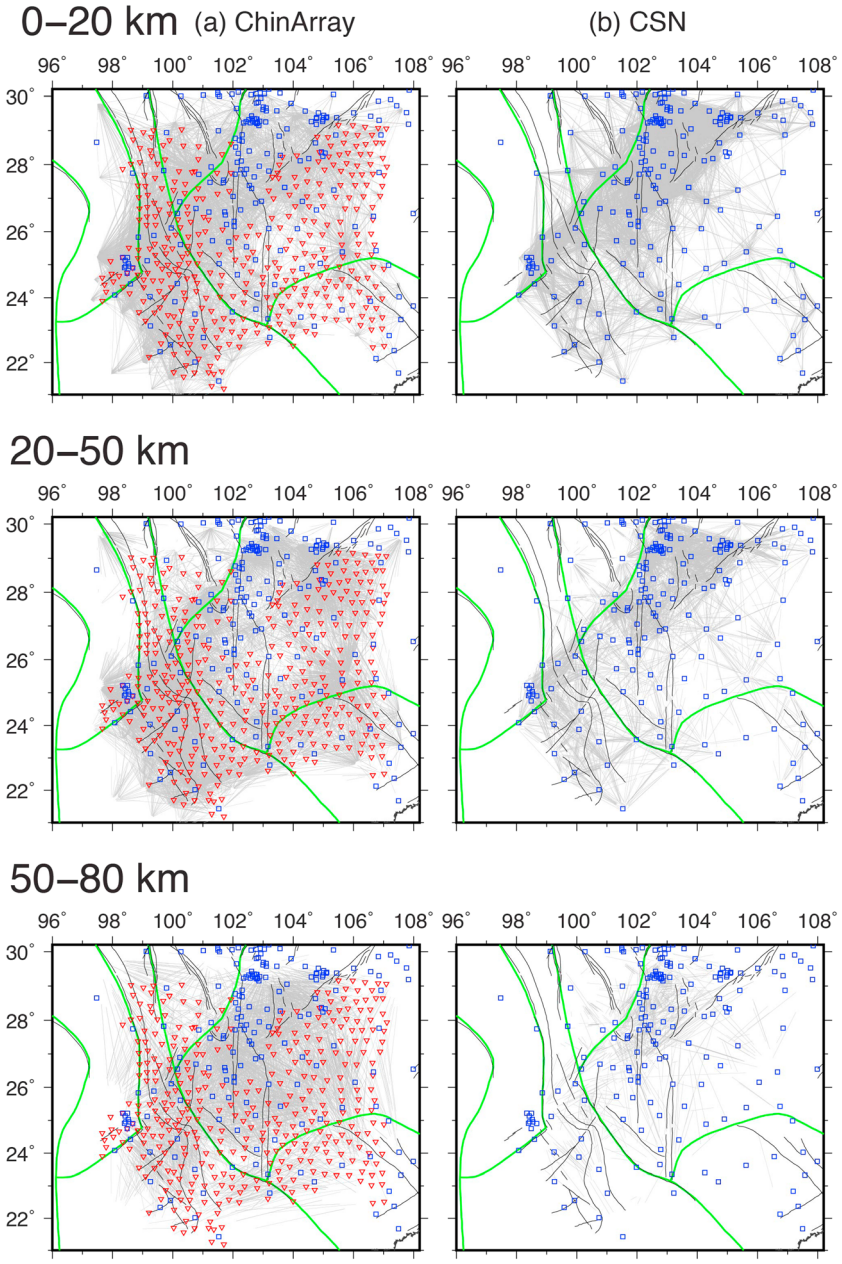

Figure 7. Distribution of the ray paths at different depth ranges from (a) the 221 events recorded at the ChinArray (red triangles) and CSN (squares) stations and (b) the 1,552 events recorded only at the CSN stations. The green and black lines denote the tectonic boundaries and active faults, respectively.

for details). Synthetic tests showed that the azimuthal anisotropy could only be well resolved when the short-to-long axis ratios of the ray ellipses are larger than 0.3; otherwise, a strong trade-off between the isotropic Vp and its anisotropy would occur (see Huang, Zhao, et al., 2015, for details). In general, the ray azimuthal coverages (Figure 8) are very good in the central part of the study region, but they are relatively poor at the edges, which would induce false structures.

The checkerboard resolution test (CRT) is efficient for evaluating the results of tomographic inversions. We first assigned positive and negative anomalies of 2% alternately to the unknown parameters (ΔS, ΔA, and ΔB) at the 3-D grid nodes, which represent the Vp azimuthal anisotropy of (α_0 = 2.83%, ψ_0 = 22.5°) and (α_0 = 2.83%, ψ_0 = 112.5°) alternately according to equations (2) and (3). We then generated synthetic data

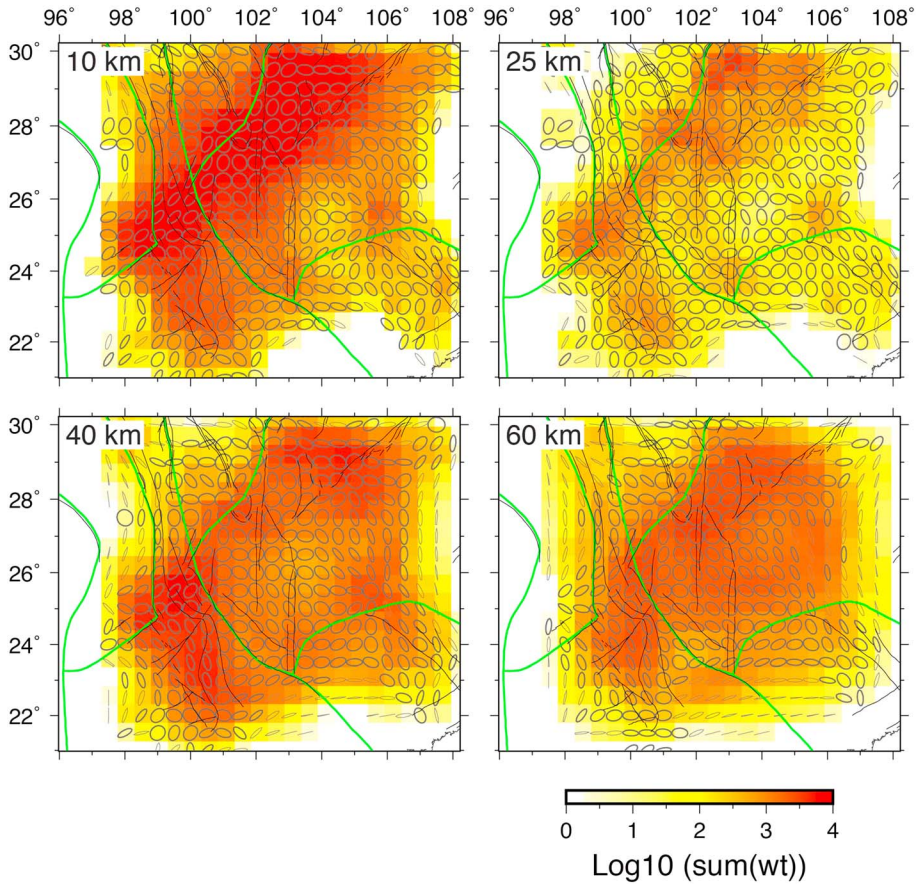

Figure 8. Distribution of the ray path density (i.e., the accumulated weights in the 3-D interpolation at the grid nodes) at four depths in the SE Tibetan Plateau. The ellipses indicate the azimuthal coverage of the subhorizontal ray segments; bold and thin ellipses denote the short-to-long axes ratios larger and smaller than 0.3, respectively (see the text for details). The green and black lines denote the tectonic boundaries and active faults, respectively.

for the checkerboard model and inverted the data (after adding random noise with a standard deviation of 0.1 s) for the checkerboard images. We used the same numbers of data as those in the real inversion, including the stations, events, and ray paths. We define a parameter for the recovery degree of azimuthal anisotropy following Huang, Zhao, et al. (2015): $R_{AA} = \left|\frac{\alpha}{\alpha_0}\cdot\cos(\psi-\psi_0)\right|$. It equals to 1 if the input anisotropy is completely recovered, while it approaches 0 if the input anisotropy is poorly recovered. We selected R_{AA} = 0.2 as the critical value above which the azimuthal anisotropy is considered well resolved according to the CRT results (Figure 10). Note that it is only an approximate and relative measure of the reliability of the obtained *P* wave azimuthal anisotropy. The CRT results suggest good recoveries at 10-, 40-, and 60-km depths for both isotropic and anisotropic structures (Figures 9 and 10), being consistent with the good ray coverages at these depths (Figures 7 and 8). At 25-km depth, the isotropic Vp structure is better recovered than the anisotropic structure.

3.2. Seismic Heterogeneity and Anisotropy

The initial root-mean-square (RMS) *P* wave traveltime residual is 0.645 s; it is reduced to 0.531 s after earthquake relocation with the 1-D velocity model (Figure 6). The RMS residual after three iterations is 0.487 s for the isotropic tomography (3-D) and 0.473 s for the anisotropic tomography (Figure 11 and Table S1 in the supporting information), which correspond to 42% and 46% reductions, respectively. It is clear that the 3-D Vp model including azimuthal anisotropy explains the traveltime data better, although the reduction of the RMS residual is small compared with that of the isotropic tomography. We conducted an *F* test (Liu & Zhao, 2016; Zhao et al., 1995) to examine the isotropic and anisotropic Vp models and the corresponding

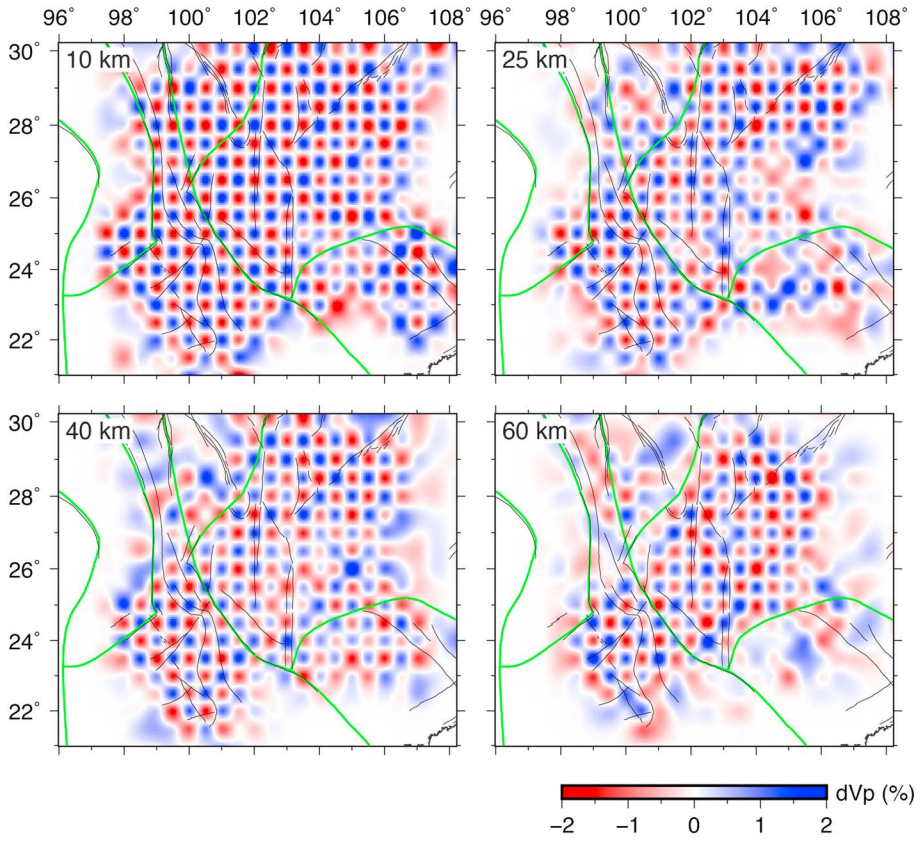

Figure 9. Results of a checkerboard resolution test for the isotropic *P* wave velocity anomalies at four depths in the SE Tibetan Plateau. The red and blue colors show the slower and faster velocity anomalies, respectively, whose scale is shown at the bottom. The green and black lines denote the tectonic boundaries and active faults, respectively.

RMS traveltime residuals, and the test result shows that the RMS residual reduction from the isotropic inversion to the anisotropic inversion is certainly significant from a statistical point of view. The small residual reduction may arise from the weak anisotropy in the medium, which is a basic assumption of the Vp anisotropic tomography. In addition, we used only part of the rays (i.e., subhorizontal ray segments as mentioned above) to constrain the *P* wave azimuthal anisotropy. The errors in the hypocentral parameters may be another factor resulting in the small RMS reduction.

The notable features are the widespread low-velocity (low-V) anomalies in the study region (Figure 11a). They are mostly located along the transition zone from a thick crust (>50 km) in the plateau to a thin crust (<40 km) in the surrounding Yangtze and Indochina Blocks. An interesting result is relatively higher velocities in the middle of the low-V zones in the deep crust (25- and 40-km depths); thus, the low-V zones are apparently constrained into belts. High-velocity (high-V) anomalies are also visible in the surrounding blocks. These features are also dominant in the Vp anisotropic tomography (Figure 11b).

The FVDs of Vp anisotropy (Figure 11b) mostly align N–S in the upper crust (10 km depth), consistent with the fault strikes. However, in the deep crust (25- and 40-km depths), the FVDs become inconsistent with the fault strikes. For example, in NW Yunnan between 26°N and 28°N where many different blocks interact, the dominant FVDs are nearly E–W, being perpendicular to the N–S faults and sutures. At 60-km depth, the FVDs rotate clockwise in the low-V zones from N–S and NE–SW along the Tibet-Yangtze boundary to E–W in NW Yunnan. The FVDs are mostly parallel to the Moho depth contour. In the surrounding regions, the FVDs are NW–SE in the Yangtze Craton and NE–SW in the Indochina Block, which are different from the FVDs in the low-V zones. The Moho in the Yangtze and Indochina Blocks is generally shallower than 50 km (Figure 3), so the tomographic results at 60-km depth generally reflect the uppermost-mantle structures there.

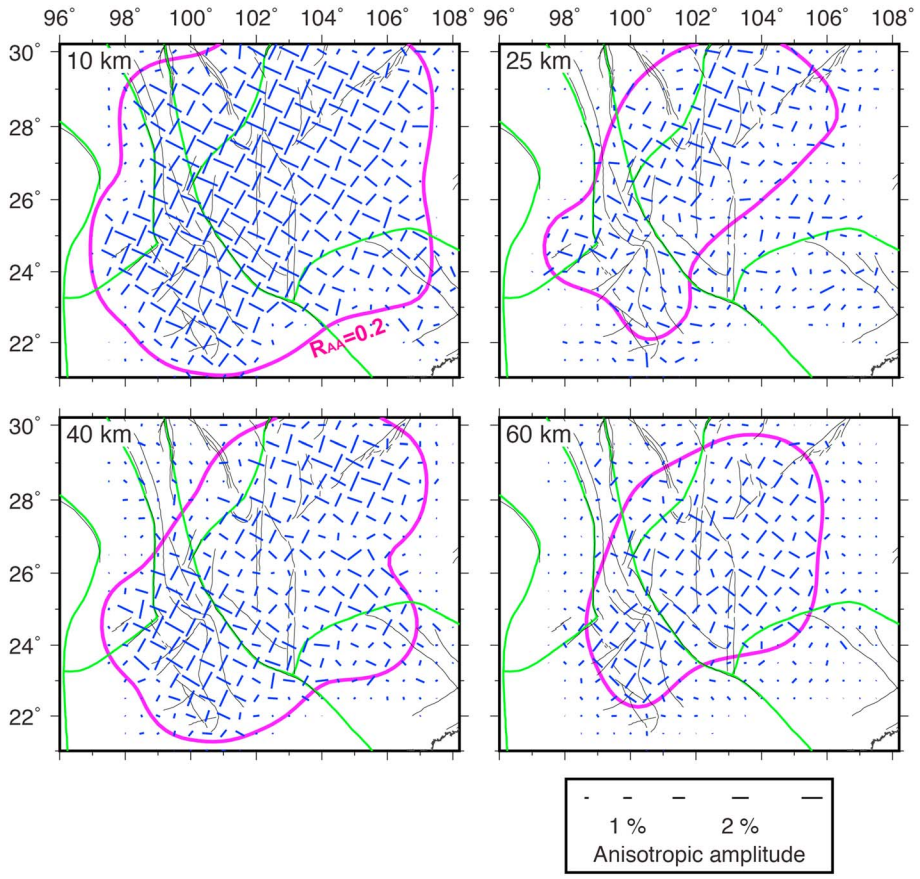

Figure 10. Results of a checkerboard resolution test for the *P* wave azimuthal anisotropy at four depths in the SE Tibetan Plateau. The orientations and lengths of the short bars denote the fast-velocity directions and anisotropic amplitudes of *P* wave azimuthal anisotropy, respectively, whose scale is shown at the bottom. The bold magenta lines marked the region where the recovery degree exceeds 0.2 (i.e., $R_{AA} \geq 0.2$; see the text for details). The green and black lines denote the tectonic boundaries and active faults, respectively.

3.3. Influence of *S* Wave Velocities

We do not invert for the 3-D *S* wave velocity (Vs) structure in this study, because the picked *S* wave arrivals are mainly *Sg* phases, and so the ray coverages in the deep crust and uppermost mantle are very poor. But the 3-D Vs structure could affect the earthquake locations significantly. Alternatively, we used a recent 3-D Vs model (Bao et al., 2015) for the crust and uppermost mantle derived from the joint inversion of receiver functions and surface wave dispersions. The average Vs of the 3-D model (Figure 6) is smaller than that of the 1-D Vs models derived from the traveltime curves. We first relocate the earthquakes with the 3-D Vs model and then conduct the same *P* wave isotropic and anisotropic tomography as described above.

The differences of the hypocentral locations between the 1-D and 3-D Vs models are significant (Figure 12). The epicentral differences are larger than 5 km for ~20% of the events and exceed 10 km for a few events. The focal depth differences are greater, over 5 km for 30% of the events and over 10 km for 10% of the events. The hypocenters derived from the 3-D Vs model are shallower than those derived from the 1-D Vs model, because the average 3-D Vs is generally smaller than the 1-D Vs (Figure 6).

The *P* wave RMS residual is reduced to 0.632 s (by 3%) after relocation with the 3-D Vs model. It is reduced to 0.586 s for the 3-D isotropic Vp model and to 0.573 s for the anisotropic 3-D Vp model (Table S2), which correspond to 17% and 21% reductions, respectively, after three iterations. Neither the new earthquake locations derived from the 3-D Vs model nor the new isotropic or anisotropic Vp models better explain the *P* wave traveltimes. This indicates that the new inversion only finds a local rather than global minimum RMS solution, as well as that using the 1-D Vs model (Figure 11). The results may be improved in the

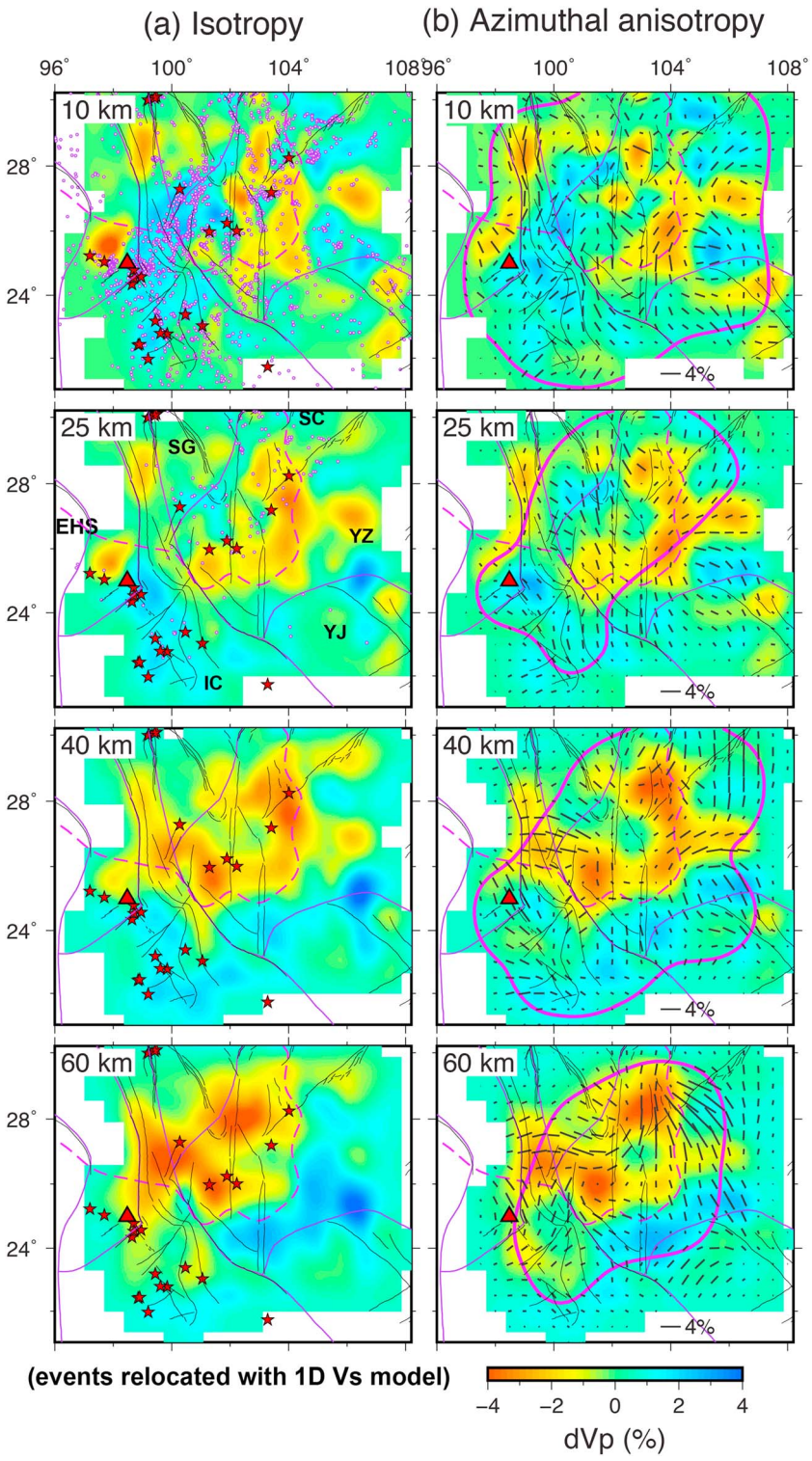

Figure 11. Map views of (a) *P* wave velocity and (b) azimuthal-anisotropy tomography at four depths in the SE Tibetan Plateau. The red and blue colors show lower and higher velocities, respectively, whose scale is shown at the bottom. The orientations and lengths of the short bars denote the fast-velocity directions and anisotropic amplitudes of *P* wave azimuthal anisotropy, respectively. The bold magenta lines marked the region where the results are reliable ($R_{AA} \geq 0.2$). The purple circles denote the background seismicity ($M \geq 3.0$; http://data.earthquake.cn). The red stars denote large crustal earthquakes ($M \geq 6.0$) occurring between 1970 and 2017 (https://earthquake.usgs.gov). The red triangle denotes the active Tengchong volcano. The purple and black lines denote the tectonic boundaries and active faults, respectively. The dashed magenta line denotes the contour line of the Moho depth at 45 km (Figure 3) for reference. See Figure 1 for the abbreviations.

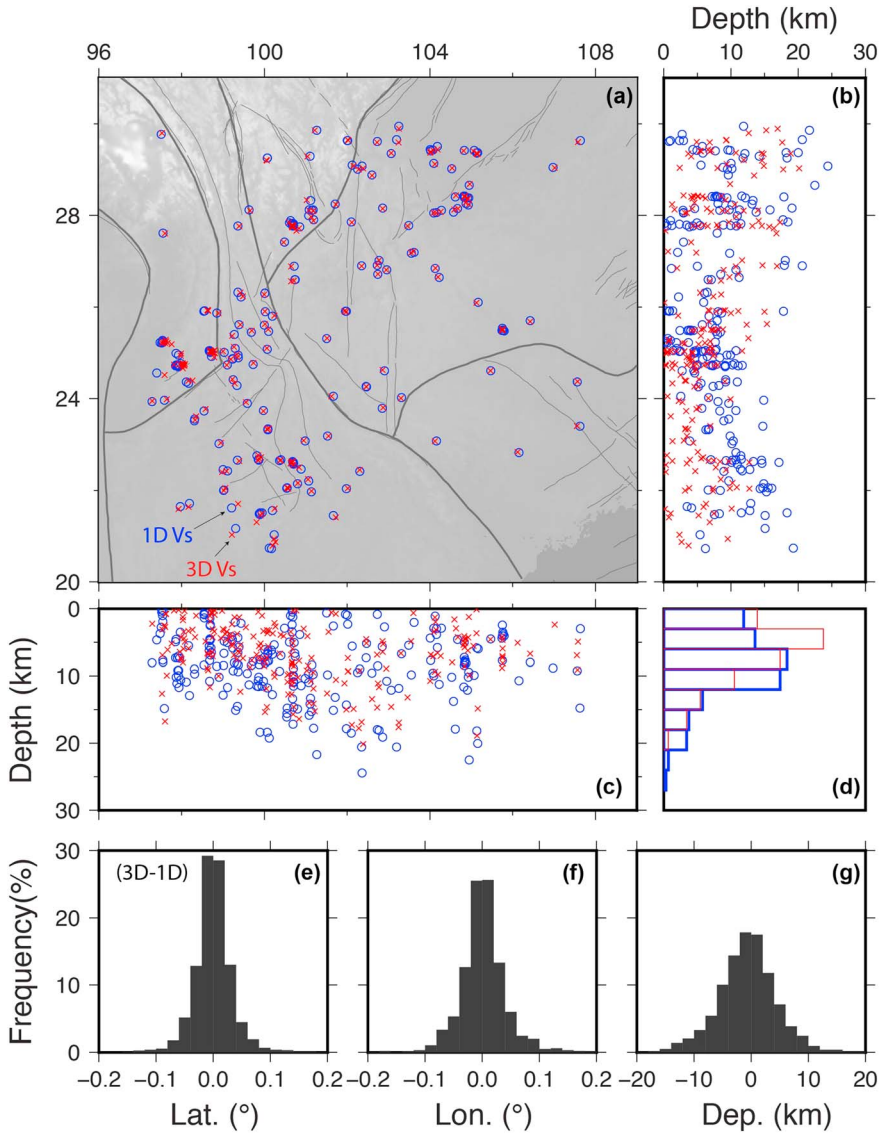

Figure 12. Comparison of the earthquake relocations with the same 1-D Vp model but different (1-D and 3-D) Vs models. The blue circles show the hypocenters relocated with the 1-D Vs model, whereas the red crosses denote the hypocenters relocated with the 3-D Vs model (Bao et al., 2015). (a–c) The comparisons in map view and E-W and N-S vertical cross-sections. (d) The statistics of the focal depths relocated with the 1-D (blue) and 3-D (red) Vs models. (e–g) The lateral and vertical differences of the hypocentral locations with the 1-D and 3-D Vs models.

future with more stations and better arrival-time data, from which the hypocentral parameters may be determined more precisely.

Anyway, we prefer the new inversion in which the 3-D Vs model is used in earthquake relocations, because the Vs model has been well determined by a joint inversion of receiver functions and surface wave tomography (e.g., Bao et al., 2015). More importantly, different studies revealed similar Vs models (e.g., Bao et al., 2015; Yao et al., 2010), suggesting that they are robust. Despite the large differences in earthquake relocations and the imperfect fitting to the *P* wave arrivals, the new isotropic and anisotropic Vp models (with the 3-D Vs model for location) show similar patterns as those in the previous models (with the 1-D Vs model for location; Figure 13), especially the *P* wave anisotropy. These similar results imply that the first-order features are reliable, and they are only slightly affected by the initial velocity models and earthquake locations. However, our new models reveal more low-V anomalies in the crust (Figure 13). In the upper crust (10-km depth), the widespread high-V zones in the Indochina Block and the Tibet-Yangtze boundary are replaced

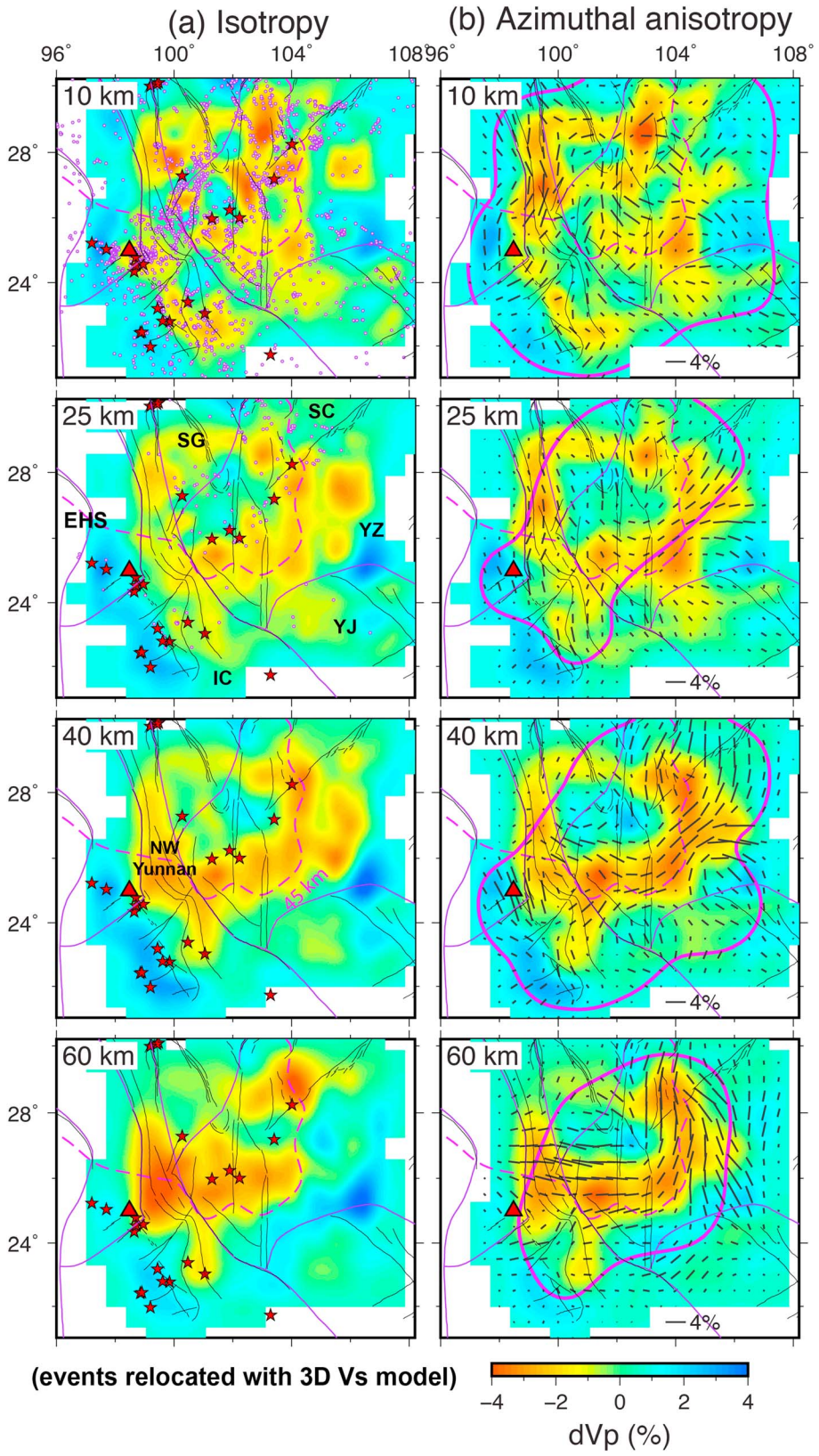

Figure 13. The same as Figure 11 but the 3-D Vs model (Bao et al., 2015) is used for earthquake relocations.

by low-V zones. The rotated FVDs in the low-V zones in the deep crust and uppermost mantle are more predominant in the new anisotropic Vp models (Figure 13).

3.4. Restoring Resolution Tests

We conducted another type of synthetic tests, the so-called restoring resolution tests (RRT), to further evaluate the isotropic Vp anomalies and azimuthal anisotropy (Figure 14). We constructed an input model for the RRT manually based on the obtained tomographic images; other steps are the same as those in the CRT. The most predominant features are the widespread low-V zones in the deep crust and the accompanying circular FVDs of the *P* wave anisotropy, as well as a high-V zone with NE–SE FVDs along the Tibet-Yangtze boundary. First, we only consider the isotropic velocity anomalies in the input model (Figure 14a). The traditional isotropic tomography could well recover the input anomalies at 40- and 60-km depths. At 25-km depth, the shapes of input anomalies are resolved while their amplitudes are smaller. Then, we apply the anisotropic tomography to the same input models to estimate the trade-off and smearing effect between the isotropic and anisotropic Vp structures (Figure 14b). In general, the isotropic anomalies are also well resolved. The Vp anisotropy due to the smearing effect is weak, mostly smaller than 1%. In some areas with poor ray (azimuthal) coverage, the anisotropic tomography could induce false Vp anisotropy up to 2%. At last, we set both isotropic and anisotropic Vp anomalies in the input models (Figure 14c). All the input anomalies are well resolved by our anisotropic tomography. These RRT results indicate that the first-order features of our results are reliable. The smearing effect may cause notable Vp anisotropy, but it does not change the general patterns (Figures 14b and 14c).

4. Discussion

4.1. Comparison With Previous Results

Previous studies have used *P* wave and surface-wave anisotropic tomography to investigate the crustal and upper-mantle anisotropy in the SE Tibetan Plateau (e.g., Huang et al., 2014; Shen et al., 2016; Wei et al., 2013; Yao et al., 2010). Huang et al. (2014) determined a 3-D regional model of Vp tomography and azimuthal anisotropy beneath Mainland China using local earthquake data recorded at the CSN stations. The lateral resolution of their model is ~200 km for the Vp anisotropy. Their results show dominant N–S FVDs in the crust (Huang et al., 2014), which are consistent with the present result and the Vs anisotropy revealed by surface-wave tomography of the Plateau (Shen et al., 2016; Yao et al., 2010). Wei et al. (2013) added more local and regional data recorded at portable stations in the SE Tibetan Plateau and also used teleseismic relative traveltime residuals. The lateral resolution of Vp anisotropy is improved to ~100 km (Wei et al., 2013). In the upper crust, the dominant N–S FVDs are very stable. At 25-km depth, the FVDs are NE–SW in general in the Yangtze Block. At depths of 40 and 60 km, NW–SE and N–S FVDs are revealed near the Tibet-Yangtze boundary and in the southwestern Yangtze Block, respectively (Wei et al., 2013). While these features are mostly visible in the present results (Figures 11 and 13), our model has a higher resolution and reveals more complex Vp anisotropy in the crust and uppermost mantle beneath the SE Tibetan Plateau. As mentioned above, the previous studies could not resolve the structures within the plateau and the Yangtze Block well due to the fewer stations and events there (Figure 7). Moreover, a surface-wave inversion revealed many E–W FVDs to the south of the Sichuan Basin (Shen et al., 2016), which are also notable in our Vp anisotropy images at depths of 25 and 40 km (Figures 11 and 13).

SWS measurements of local S and Pms (P-to-S converted wave at the Moho) phases provide important information on the crustal anisotropy. The SWS method has a high lateral resolution but a poor vertical resolution. The local *S* wave splitting mostly reflects the upper-crustal anisotropy because the earthquakes mostly occurred in the upper crust. The Pms splitting results from crustal anisotropy between the surface and the Moho; the difference between the local *S* and Pms splitting measurements could provide information on the lower-crustal anisotropy. The polarization directions of the fast *S* waves (FPDs; comparable to FVD for Vp anisotropy) usually align N–S and are parallel to the fault strikes (Figure 15a; Shi et al., 2012). The delay times between the fast and slow *S* waves are ~0.1 s. The Pms splitting measurements also show dominant N–S FPDs that are consistent with the local *S* wave splitting and the fault strikes (Figure 15b; Cai et al., 2016; Chen et al., 2013; Sun et al., 2012). The delay times mostly range between 0.2 and 0.4 s but reach ~0.5 s at many stations, suggesting strong anisotropy in the lower crust. The Pms splitting FPDs deviate from the fault strikes significantly in some areas. The first one is in northwest Yunnan, where the E–W FPDs are

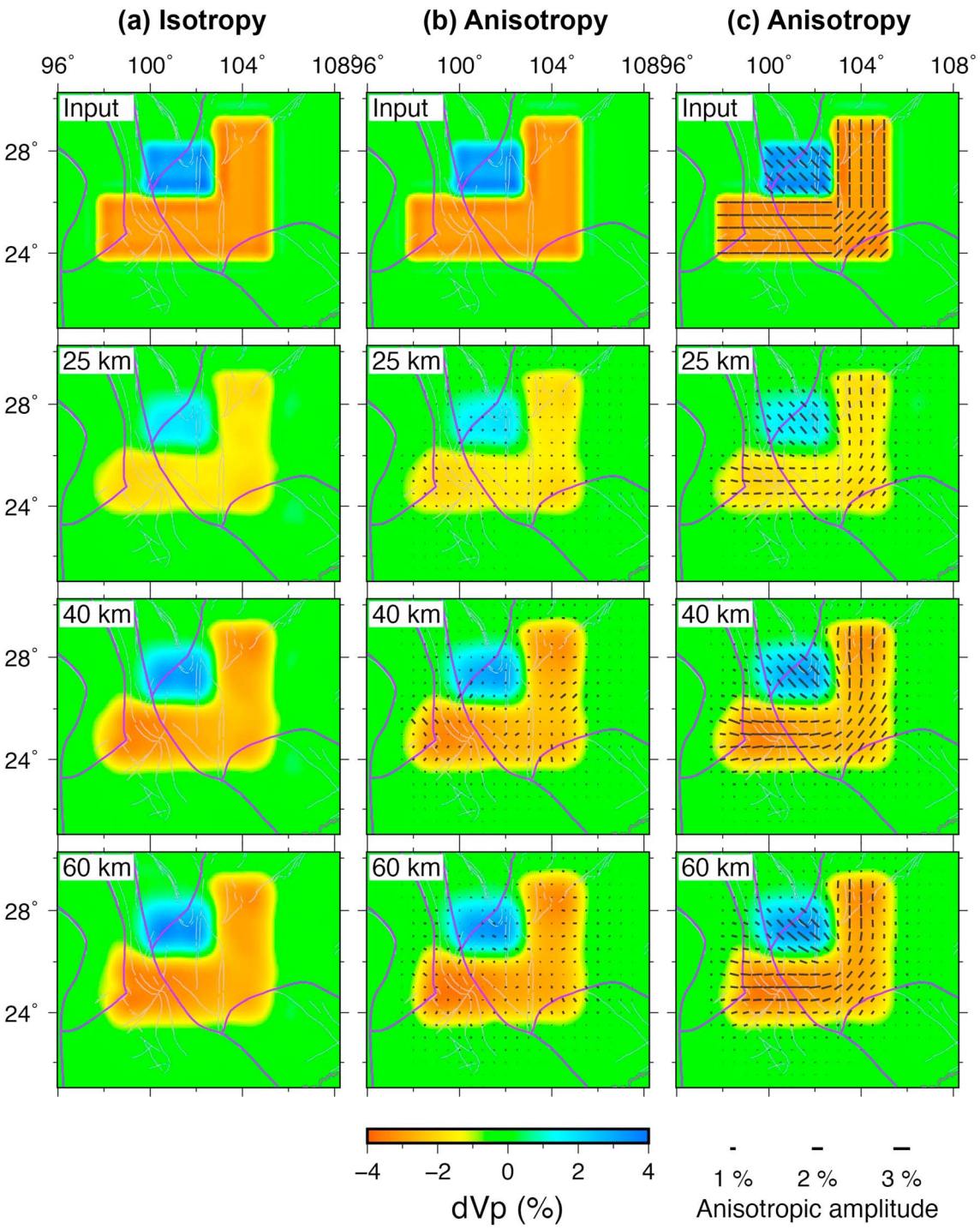

Figure 14. Results of restoring resolution tests for the dominant *P* wave velocity and azimuthal anisotropy revealed by this study. From top to bottom are the input models and the inverted results at 25-, 40-, and 60-km depths. (a) The test for the *P* wave velocity anomalies with the isotropic tomography. (b) The input model is the same as (a) but inverted with the *P* wave anisotropic tomography. (c) The same as (b) but initial *P* wave anisotropy is included in the input model.

perpendicular to the surface faults and sutures (Figure 15b) but parallel with our Vp FVDs in the deep crust (Figures 11 and 13). Another region is near the Xiaojiang fault, where the dominant NE–SW FVDs deviate from the N–S fault strike (Figure 15b). These observations are well correlated with our Vp anisotropy in the deep crust and uppermost mantle.

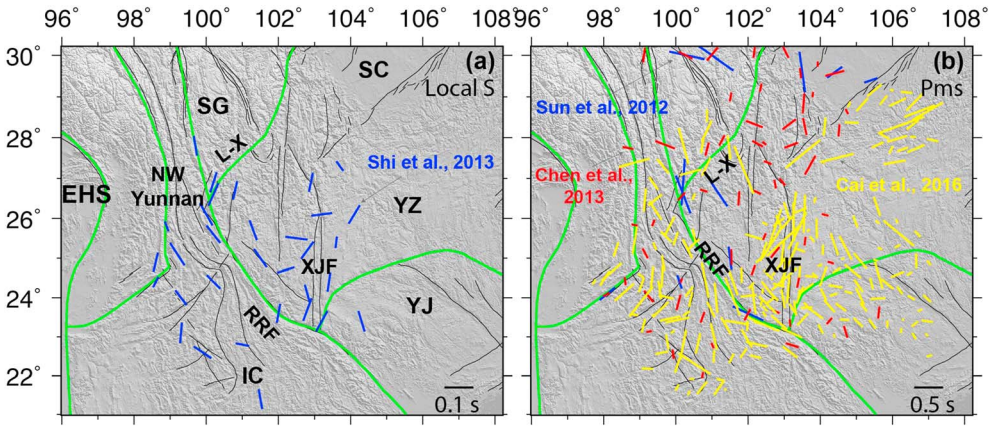

Figure 15. (a) Local *S* wave splitting measurements for the crustal earthquakes (Shi et al., 2012) supposing a 20-km-thick anisotropic layer. (b) Pms splitting measurements by previous studies (Cai et al., 2016; Chen et al., 2013; Sun et al., 2012). The orientations and lengths of the short bars denote the polarization directions of the fast wave and the delay times, respectively. Note different scales for the delay times shown at the bottom right. The green and black lines denote the tectonic boundaries and active faults, respectively. See Figure 1 for the abbreviations.

4.2. Crustal and Upper-Mantle Deformations

The overall FVDs in the upper crust are generally parallel to the strikes of active faults (Figures 11 and 13), which result from the aligned cracks and fabrics accompanying the fault activities (e.g., Babuska & Cara, 1991; Crampin & Chastin, 2003). The FVDs in the lower crust and uppermost mantle show different patterns, deviating from the fault strikes significantly (Figures 11 and 13). The deformations in the deep crust seem independent of the upper-crust deformations and fault activities.

However, the upper-crustal stress field in the SE Tibetan Plateau (Figure 16) inverted from focal mechanism solutions and global position system (GPS) observations shows a comparable pattern to the rotated FVDs in the deep crust and uppermost mantle (e.g., Xu et al., 2016; Zhao et al., 2013). The orientations of the maximal horizontal extension (Sh; Figure 16) change from roughly N–S near the Tibet-Sichuan boundary to NE–SW in the southwest Yangtze Craton, further to E–W in the northern Indochina Block, and finally to NW–SE in front of the eastern Himalayan syntax. The Sh orientations are generally parallel to the topographic contour lines while perpendicular to the topographic gradients. The good correlations imply that the gravitational potential controls the stress and strain fields in the upper crust in the SE Tibetan Plateau. If the strain fields continue in the deep crust and upper mantle, the minerals will be aligned so that their lattice preferred orientations are parallel to the extensional directions (i.e., Sh; e.g., Karato et al., 2008; Ko & Jung, 2015). Thus, the *P* wave FVDs will show the same rotation as the Sh orientations, as shown in our tomographic images (Figures 11 and 13). These results support the fact that the gravitational potential plays an important role in the deep-crustal and uppermost-mantle deformations in the SE Tibetan Plateau, which could produce the first-order pattern of seismic anisotropy there.

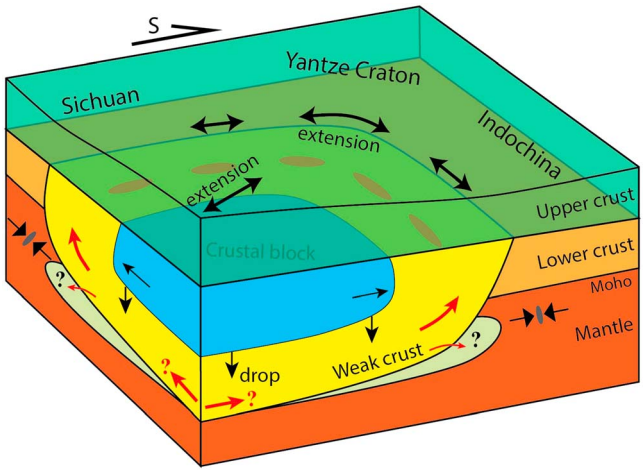

Figure 16. A 3-D block model of sinking crustal block in SE Tibetan Plateau. Red arrows denote possible ductile crustal flow or intrusion. Black arrows denote movement and drop of the crustal block proposed by this study. Double-head arrows show the horizontal extension obtained by a stress tensor inversion (Xu et al., 2016).

Because the Moho depth is 30–50 km in the Yangtze and Indochina Blocks (Figure 3; Wang et al., 2017), the *P* wave azimuthal anisotropy at 40- and 60-km depths may largely reflect the uppermost-mantle structures. We can hardly discriminate the crustal and upper-mantle structures clearly. The southwest Yangtze Block belongs to a Permian large igneous province (Figure 1; Ali et al., 2005; Xu et al., 2017). There are large magma chambers, many magma channels, and periods of magmatic intrusion in the lithosphere. Thus, the crust and upper mantle may retain some similar fossil magmatic inclusions and structures. In fact, a previous study revealed a transitional crust-mantle boundary in eastern Tibet (Liu et al., 2014) and proposed possible deep-crustal intrusion into the upper mantle.

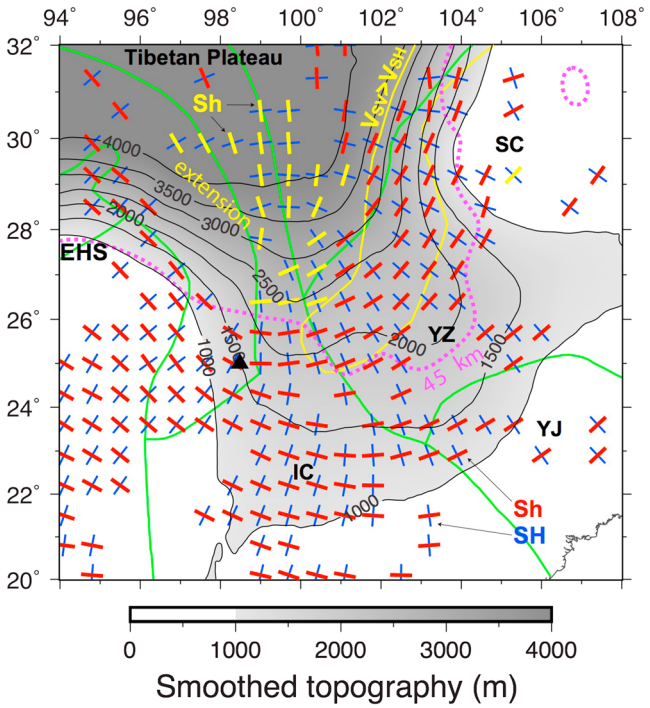

Figure 17. The blue bars show the maximum horizontal stresses (SH) in the SE Tibetan Plateau (Xu et al., 2016). The yellow bars show the minimal horizontal stresses (Sh; i.e., maximum extension) in an extensional environment while the red bars show the Sh orientations in thrust and strike-slip environments. The gray colors with contours denote the surface elevations. The green lines denote the tectonic boundaries. The yellow line indicates the area with a negative radial anisotropy ($V_{SV} > V_{SH}$) throughout the crust (Xie et al., 2017). The dashed magenta line denotes the 45-km depth contour of the Moho (Figure 3) for reference. See Figure 1 for the other abbreviations.

Therefore, the deep crust and uppermost mantle in the SE Tibetan Plateau are not so different from those of typical cratons, and they may have similar compositions and have experienced similar deformations, resulting in similar features of seismic anisotropy.

The structures beneath the Tibet-Yangtze boundary argue for an additional mechanism in the SE Tibetan Plateau beside the gravitational potential. A notable high-V body is revealed in the middle of the low-V zones in the deep crust (Figures 11 and 13), also notable in the surface wave tomography (e.g., Bao et al., 2015; Yao et al., 2010). The FVDs in the high-V body are complex, without preferred directions. The heat flow is very low, smaller than 60 mW/m^2, in this region (Hu et al., 2000), which is only about half of those in the surrounding areas (Figure 17). Geological surveys identified the Muli and Jinhe-Qinghe thrust zones in the Cenozoic (Figure 1; China Geology Survey, 2002; Wang et al., 2012). However, the current crust is subsiding, in contrast to significant uplift around it (Figure 17; Liang et al., 2013; Pan & Shen, 2017).

We propose that shallow-crustal materials may sink into the ductile deep crust in the region (Figure 16). The low-V anomalies with a high conductivity may reflect partial melting and weak mid-lower crust beneath the eastern Tibetan Plateau (Bai et al., 2010; Bao et al., 2015; Wei et al., 2001; Yao et al., 2010). Thus, accompanying the thrusts in the upper crust, a significant portion of the shallow-crustal materials (or block) may sink into the deep crust due to the gravitational potential. This process also explains a locally extensional region in the high plateau to the northwest (Figure 17; Xu et al., 2016; Zhao et al., 2013). It could also produce notably negative radial anisotropy ($V_{SH} < V_{SV}$) in the deep crust along the Tibet-Yangtze boundary (Figures 17 and 18; Xie et al., 2017). The deep crust usually exhibits horizontal extension under gravity loading because the mid-lower crust has lower velocities and is considered weak (e.g., Beaumont et al., 2001; Hacker et al., 2014; Shapiro et al., 2004), resulting in widespread positive radial anisotropies (i.e., $V_{SH} > V_{SV}$). In contrast, the upper crust is dominated by negative radial anisotropy (i.e., $V_{SH} < V_{SV}$) due to subvertical hexagonal fabrics under the Indo-Asian convergence (Xie et al., 2017). If the shallow crust drops, the original positive radial anisotropy in the deep crust will be broken and replaced by the frozen anisotropy in the dropped crustal block.

The dropped crustal block can drive ductile deep-crustal material to intrude into the adjacent regions (Figure 16). However, the deep Moho under the plateau extends into the Yangtze Craton like a tongue southeastward (Figure 3). The Moho depth changes by 20 km from the SE Tibetan Plateau to the surrounding Yangtze and Indochina Blocks (Figure 3). Thus, the deep-crustal materials extruded by the dropped shallow crust are more likely to be trapped in this tongue-shaped corner (Figure 16). The FVDs in this case are parallel to the Moho depth contour, which is actually a significant feature of our *P* wave anisotropy (Figures 11 and 13). The accumulated and trapped ductile crust may be extruded upward eventually into the shallow crust (e.g., Beaumont et al., 2001; Li et al., 2015), as indicated by the low-V zones extending to the upper crust (Figures 11 and 13). This process has caused significant upper-crustal uplift and high heat flow at the surface (Figure 18; Hu et al., 2000; Liang et al., 2013; Pan & Shen, 2017).

The deep-crustal extrusion (due to the shallow-crustal drop) indicates different deformations in the shallow and deep crust in the study region. GPS observations suggest dominant sinistral slips and strong deformations along the Xianshuihe-Anninghe-Xiaojiang and Lijiang-Xiaojinhe faults in the SE Tibetan Plateau (Figure 2b; e.g., Kreemer et al., 2014; Pan & Shen, 2017). However, significant uplift does not occur along these faults (Figure 18; Gan et al., 2007; Liang et al., 2013; Zheng et al., 2017), arguing for deep-crustal contributions rather than shallow-crustal deformation as discussed above.

The distribution of deep-crustal extrusion may influence the seismotectonics in the SE Tibetan Plateau, especially within the Yangtze Craton. Large earthquakes ($M \geq 6.0$) generally occurred to the northwest of a NE–SW

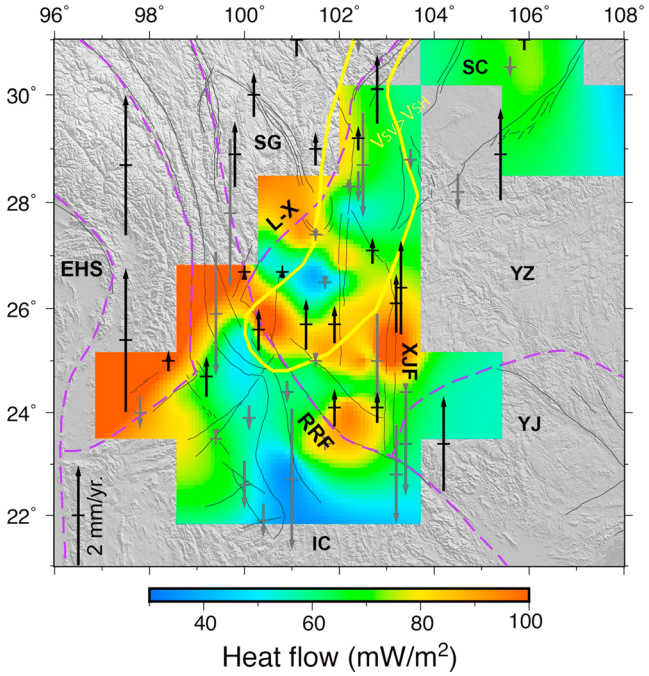

Figure 18. Distribution of the crustal vertical motions (Pan & Shen, 2017) and surface heat flow (Hu et al., 2000) in the SE Tibetan Plateau. The color scale for the heat flow is shown at the bottom. The black and gray vertical arrows denote the surface uplift and subsidence, respectively. The yellow line shows the area with a negative radial anisotropy ($V_{SH} < V_{SV}$) throughout the crust (Xie et al., 2017). For the abbreviations, see Figure 1.

belt (earthquake front; Figure 3), which are located around the low-V zones in the crust (Figures 11 and 13). The deep-crustal extrusion probably weakens the cratonic crust and makes the large crustal earthquakes easier to occur (e.g., Wei et al., 2013). On the other hand, earthquakes did not occur in the low-V zones in the upper crust, which may represent very hot and weak materials extruded from the deep crust or heated by the deep-crustal flow (e.g., Beaumont et al., 2001; Li et al., 2015). Therefore, in the low-V areas the stress is not apt to accumulate to generate large earthquakes; the energy is released by ductile aseismic deformation. The low-V zones prevent the stress from transferring eastward to the stable Yangtze Craton.

The deep-crustal flow model is one of the popular models for explaining the tectonic evolution of the Tibetan Plateau (e.g.,Clark et al., 2005 ; Royden et al., 2008), which accounts for the eastern Tibetan uplift well with little upper-crustal shortening. We cannot prove or rule out deep-crustal flow originating from the high plateau beneath the SE Tibetan Plateau. The present Vp isotropic and anisotropic models can explain the shallow-crustal drop into the deep crust. Superimposing the process on deep-crustal flow will enhance the extruded crustal flow and the circular FVDs but without significant difference. In the deep-crustal flow, preferred orientations of the minerals (e.g., mica and amphibole) and partial-melting inclusions generally produce flow-parallel FVDs (e.g., Ji et al., 2015; Ko & Jung, 2015), that is, NW–SE in the SE Tibetan Plateau. They seem visible at 25- and 40-km depths in our images of Vp anisotropy inverted with earthquake locations in the 1-D Vs model (Figure 11) but disappear in the images of Vp anisotropy with the 3-D Vs model (Figure 13). Hence, the flow-parallel FVDs are not a robust feature, because they are affected by the earthquake locations. More detailed information on the 3-D crustal anisotropy in the Tibetan Plateau is necessary to clarify this issue. However, we prefer the existence of the deep-crustal flow, because the plateau uplift in the northwestern part of the study region is notable (Figure 18; Liang et al., 2013; Pan & Shen, 2017). The focal mechanism solutions indicate that the upper crust is undergoing horizontal extension (Figure 17; Xu et al., 2016; Zhao et al., 2013); hence, the plateau uplift cannot be caused by upper-crustal deformations. The thickened ductile deep crust is a more plausible explanation (Clark et al., 2005; Royden et al., 2008).

4.3. Implications for SWS Measurements

Many SWS measurements have been made in the SE Tibetan Plateau (e.g., Huang et al., 2007; Huang, Wang, et al., 2015; Lev et al., 2006; Sol et al., 2007; Wang et al., 2008), which are generally interpreted to result from lithospheric and asthenospheric deformations (e.g., Long & Silver, 2009; Silver & Chan, 1991). There is a predominant change in the SWS FPDs from N–S in the north to E–W in the south across 26–27°N. Previous studies debated whether the deformations in the crust and upper mantle are coupled or not (e.g., León Soto et al., 2012; Sol et al., 2007; Wang et al., 2008). Sol et al. (2007) compared the GPS-derived surface sinistral strain and the SWS FPDs and proposed decoupled crust and upper-mantle deformations. However, more comprehensive later studies inverted the GPS measurements for the sinistral, dextral strain and maximum extension field in the shallow crust (e.g., León Soto et al., 2012; Wang et al., 2008). The SWS FPDs are found to be subparallel to the crustal extension, suggesting that the crust and upper mantle in the SE Tibetan Plateau are under gravity-driven compression coherently (e.g., León Soto et al., 2012; Wang et al., 2008). The SWS measurements may also be affected by the asthenospheric anisotropy due to the mantle flow arising from the plateau or driven by the absolute plate motions and the Indian plate subduction (e.g., Huang, Wang, et al., 2015).

The *P* wave azimuthal anisotropy (Figures 11 and 13) provides important constraints on the anisotropy in the crust and uppermost mantle. There are very good correlations between the Vp anisotropy FVDs and the SWS FPDs in certain areas. The dominant N–S FVDs in the crust (10- and 25-km depths) are similar to the splitting

FPDs in the plateau. In the Yangtze Block, the abrupt change of FPDs at ~27°N is also notable in the present Vp anisotropy at 25- and 40-km depths. The dominant E–W FPDs to the south of 26°N are parallel to our Vp anisotropy at 60-km depth. These correlations indicate significant contributions of the anisotropy in the crust and uppermost mantle to the SWS measurements.

However, the first-order feature of the SWS FPDs, that is, the change from N–S in the north to E–W in the south (e.g., Huang, Wang, et al., 2015; Lev et al., 2006; Sol et al., 2007; Wang et al., 2008), is not notable in the Vp anisotropy. At 40- and 60-km depths, circular FVDs are revealed along the southeastern plateau margin and the contour line of the Moho depth (Figure 11). For an average Vs of 3.5 km/s (Figure 6) with 4% anisotropy, a 35-km-thick crust could produce a maximum SWS delay time of 0.4 s, comparable to the Pms splitting measurements (Figure 15b; Cai et al., 2016; Chen et al., 2013; Sun et al., 2012). Even for a 70-km-thick crust beneath the high plateau (Figure 3), the maximum delay time is no more than 0.8 s (being overestimated because of the underestimated Vs), at most half of the SWS observations (e.g., Huang, Wang, et al., 2015; Wang et al., 2008). These discrepancies argue for other important sources of anisotropy from the deeper mantle. In particular, under the northern Indochina Block, the lithospheric thickness is only ~50 km (e.g., An & Shi, 2006; Pasyanos et al., 2014), producing a maximum SWS delay time of 0.5 s. The remaining 1.0-s delay time argues for the sublithospheric (i.e., asthenospheric) anisotropy.

5. Conclusions

We collected a large number of *P* and *S* wave arrival times from seismograms of local earthquakes recorded by a dense seismic array deployed in the SE Tibetan Plateau and then used the data to determine a high-resolution 3-D model of *P* wave tomography and azimuthal anisotropy of the crust and uppermost mantle. Our new data set significantly improves the ray coverage and resolution in the deep crust and the uppermost mantle beneath the study region. Our results reveal widespread low-V zones around a high-V body in the deep crust and uppermost mantle beneath the southwest Yangtze Craton. The FVDs in the low-V zones rotate clockwise and are parallel to the plateau margin and the contour lines of the Moho depth. While the gravitational potential could produce the first-order pattern of the obtained *P* wave anisotropy, our tomographic images indicate that an upper-crustal block has dropped to the deep crust beneath the SE Tibetan Plateau. The dropped crustal block drives the ductile deep crust to intrude into the southwest Yangtze Craton that has been destructed by major Permian volcanic activity. On the other hand, the extruded crustal flow is accumulated and trapped in a tongue-shaped deep-crust corner in the SE Tibetan Plateau due to the resistance of the surrounding blocks. The trapped flow tends to extrude upward, causing local uplift and high heat flow at the surface. It could also intrude downward into the upper mantle to strengthen the deformation there in addition to the gravitational potential.

Acknowledgments
The waveform data were provided by the China Seismic Array Data Management Center at the Institute of Geophysics, China Earthquake Administration (http://www.chinaarray.org). We thank the China Seismic Network data center for providing part of the arrival-time data used in this study (http://data.earthquake.cn). Comments from Prof. M. Savage (the Editor), the Associate Editor, and three anonymous reviewers have greatly improved the paper. This work was supported by the National Key Research and Development Program of China (Grants 2017YFC0601406), the National Natural Science Foundation of China (41674044 and 41674049) and by the ChinArray Program (DQJB16A0306). Z. H. has been supported by the Alexander von Humboldt-Stiftung and the Deng Feng Scholar Program of Nanjing University. Most figures were made using GMT (Wessel et al., 2013).

References

Ali, J. R., Thompson, G. M., Zhou, M.-F., & Song, X. (2005). Emeishan large igneous province, SW China. *Lithos*, *79*(3–4), 475–489. https://doi.org/10.1016/j.lithos.2004.09.013

An, M., & Shi, Y. (2006). Lithospheric thickness of the Chinese continent. *Physics of the Earth and Planetary Interiors*, *159*(3–4), 257–266. https://doi.org/10.1016/j.pepi.2006.08.002

Babuska, V., & Cara, M. (1991). *Seismic anisotropy in the Earth*. Netherlands: Springer. Springer-Science+Business Media, B.V, DOI: https://doi.org/10.1007/978-94-011-3600-6

Babuška, V., Plomerová, J., & Šílený, J. (1993). Models of seismic anisotropy in the deep continental lithosphere. *Physics of the Earth and Planetary Interiors*, *78*(3-4), 167–191. https://doi.org/10.1016/0031-9201(93)90154-2

Bai, D., Unsworth, M. J., Meju, M. A., Ma, X., Teng, J., Kong, X., et al. (2010). Crustal deformation of the eastern Tibetan Plateau revealed by magnetotelluric imaging. *Nature Geoscience*, *3*(5), 358–362. https://doi.org/10.1038/ngeo830

Bao, X., Sun, X., Xu, M., Eaton, D. W., Song, X., Wang, L., et al. (2015). Two crustal low-velocity channels beneath SE Tibet revealed by joint inversion of Rayleigh wave dispersion and receiver functions. *Earth and Planetary Science Letters*, *415*, 16–24. https://doi.org/10.1016/j.epsl.2015.01.020

Beaumont, C., Jamieson, R. A., Nguyen, M. H., & Lee, B. (2001). Himalayan tectonics explained by extrusion of a low-viscosity crustal channel coupled to focused surface denudation. *Nature*, *414*(6865), 738–742. https://doi.org/10.1038/414738a

Cai, Y., Wu, J., Fang, L., Wang, W., & Yi, S. (2016). Crustal anisotropy and deformation of the southeastern margin of the Tibetan Plateau revealed by Pms splitting. *Journal of Asian Earth Sciences*, *121*, 120–126. https://doi.org/10.1016/j.jseaes.2016.02.005

Calvet, M., Chevrot, S., & Souriau, A. (2006). P-wave propagation in transversely isotropic media. I. Finite-frequency theory. *Physics of the Earth and Planetary Interiors*, *156*(1–2), 12–20. https://doi.org/10.1016/j.pepi.2006.01.004

Chen, Y., Zhang, Z., Sun, C., & Badal, J. (2013). Crustal anisotropy from Moho converted Ps wave splitting analysis and geodynamic implications beneath the eastern margin of Tibet and surrounding regions. *Gondwana Research*, *24*(3–4), 946–957. https://doi.org/10.1016/j.gr.2012.04.003

China Geology Survey (2002). *Geological map of the People's Republic of China (1:2 500 000)*. Beijing: Sinomaps Press.

Clark, M. K., House, M. A., Royden, L. H., Whipple, K. X., Burchfiel, B. C., Zhang, X., & Tang, W. (2005). Late Cenozoic uplift of southeastern Tibet. *Geology*, *33*(6), 525–528. https://doi.org/10.1130/G21265.1

Clark, M. K., & Royden, L. H. (2000). Topographic ooze: Building the eastern margin of Tibet by lower crustal flow. *Geology*, *28*(8), 703–706. https://doi.org/10.1130/0091-7613(2000)28<703:TOBTEM>2.0.CO;2

Crampin, S., & Chastin, S. (2003). A review of shear wave splitting in the crack-critical crust. *Geophysical Journal International*, *155*(1), 221–240. https://doi.org/10.1046/j.1365-246X.2003.02037.x

Crotwell, H. P., Owens, T. J., & Ritsema, J. (1999). The TauP toolkit: Flexible seismic travel-time and ray-path utilities. *Seismological Research Letters*, *70*(2), 154–160. https://doi.org/10.1785/gssrl.70.2.154

Deng, Q., Zhang, P., Ran, Y., Yang, X., Min, W., & Chu, Q. (2003). Basic characteristics of active tectonics of China. *Science in China Series D: Earth Sciences*, *46*(4), 356–372. https://doi.org/10.1360/03yd9032

Eberhart-Phillips, D., & Henderson, C. M. (2004). Including anisotropy in 3-D velocity inversion and application to Marlborough, New Zealand. *Geophysical Journal International*, *156*(2), 237–254. https://doi.org/10.1111/j.1365-246X.2003.02044.x

Eberhart-Phillips, D., & Reyners, M. (2009). Three-dimensional distribution of seismic anisotropy in the Hikurangi subduction zone beneath the central North Island, New Zealand. *Journal of Geophysical Research*, *114*, B06301. https://doi.org/10.1029/2008JB005947

Engdahl, E. R., & Lee, W. H. K. (1976). Relocation of local earthquakes by seismic ray tracing. *Journal of Geophysical Research*, *81*(23), 4400–4406. https://doi.org/10.1029/JB081i023p04400

England, P., & Houseman, G. (1986). Finite strain calculations of continental deformation: 2. Comparison with the India-Asia collision zone. *Journal of Geophysical Research*, *91*(B3), 3664–3676. https://doi.org/10.1029/JB091iB03p03664

Gan, W., Zhang, P., Shen, Z.-K., Niu, Z., Wang, M., Wan, Y., et al. (2007). Present-day crustal motion within the Tibetan Plateau inferred from GPS measurements. *Journal of Geophysical Research*, *112*, B08416. https://doi.org/10.1029/2005JB004120

Hacker, B. R., Ritzwoller, M. H., & Xie, J. (2014). Partially melted, mica-bearing crust in Central Tibet. *Tectonics*, *33*, 1408–1424. https://doi.org/10.1002/2014TC003545

Hu, S., He, L., & Wang, J. (2000). Heat flow in the continental area of China: A new data set. *Earth and Planetary Science Letters*, *179*(2), 407–419. https://doi.org/10.1016/S0012-821X(00)00126-6

Huang, Z., Wang, L., Xu, M., Ding, Z., Wu, Y., Wang, P., et al. (2015). Teleseismic shear-wave splitting in SE Tibet: Insight into complex crust and upper-mantle deformation. *Earth and Planetary Science Letters*, *432*, 354–362. https://doi.org/10.1016/j.epsl.2015.10.027

Huang, Z., Wang, L., Xu, M., Liu, J., Mi, N., & Liu, S. (2007). Shear wave splitting across the Ailao Shan-Red River fault zone, SW China. *Geophysical Research Letters*, *34*, L20301. https://doi.org/10.1029/2007GL031236

Huang, Z., Wang, P., Zhao, D., Wang, L., & Xu, M. (2014). Three-dimensional P wave azimuthal anisotropy in the lithosphere beneath China. *Journal of Geophysical Research: Solid Earth*, *119*, 5686–5712. https://doi.org/10.1002/2014JB010963

Huang, Z., Zhao, D., & Liu, X. (2015). On the trade-off between seismic anisotropy and heterogeneity: Numerical simulations and application to Northeast Japan. *Journal of Geophysical Research: Solid Earth*, *120*, 3255–3277. https://doi.org/10.1002/2014JB011784

Huang, Z., Zhao, D., & Wang, L. (2011). Seismic heterogeneity and anisotropy of the Honshu arc from the Japan Trench to the Japan Sea. *Geophysical Journal International*, *184*(3), 1428–1444. https://doi.org/10.1111/j.1365-246X.2011.04934.x

Ji, S., Shao, T., Michibayashi, K., Oya, S., Satsukawa, T., Wang, Q., et al. (2015). Magnitude and symmetry of seismic anisotropy in mica- and amphibole-bearing metamorphic rocks and implications for tectonic interpretation of seismic data from the southeast Tibetan Plateau. *Journal of Geophysical Research: Solid Earth*, *120*, 6404–6430. https://doi.org/10.1002/2015JB012209

Karato, S.-I., Jung, H., Katayama, I., & Skemer, P. (2008). Geodynamic significance of seismic anisotropy of the upper mantle: New insights from laboratory studies. *Annual Review of Earth and Planetary Sciences*, *36*(1), 59–95. https://doi.org/10.1146/annurev.earth.36.031207.124120

Kennett, B., Engdahl, E. R., & Buland, R. (1995). Constraints on seismic velocities in the Earth from travel-times. *Geophysical Journal International*, *122*(1), 108–124. https://doi.org/10.1111/j.1365-246X.1995.tb03540.x

Kind, R., Yuan, X., Saul, J., Nelson, D., Sobole, S. V., Mechie, J., et al. (2002). Seismic images of crust and upper mantle beneath Tibet: Evidence for Eurasian Plate subduction. *Science*, *298*(5596), 1219–1221. https://doi.org/10.1126/science.1078115

Ko, B., & Jung, H. (2015). Crystal preferred orientation of an amphibole experimentally deformed by simple shear. *Nature Communications*, *6*(1). https://doi.org/10.1038/ncomms7586

Kreemer, C., Blewitt, G., & Klein, E. C. (2014). A geodetic plate motion and global strain rate model. *Geochemistry, Geophysics, Geosystems*, *15*, 3849–3889. https://doi.org/10.1002/2014GC005407

Lees, J. M., & Crosson, R. S. (1989). Tomographic inversion for three-dimensional velocity structure at Mount St. Helens using earthquake data. *Journal of Geophysical Research*, *94*(B5), 5716. https://doi.org/10.1029/jb094ib05p05716

León Soto, G., Sandvol, E., Ni, J. F., Flesch, L., Hearn, T. M., Tilmann, F., et al. (2012). Significant and vertically coherent seismic anisotropy beneath eastern Tibet. *Journal of Geophysical Research*, *117*, B05201. https://doi.org/10.1029/2011JB008919

Lev, E., Long, M., & Vanderhilst, R. (2006). Seismic anisotropy in eastern Tibet from shear wave splitting reveals changes in lithospheric deformation. *Earth and Planetary Science Letters*, *251*(3–4), 293–304. https://doi.org/10.1016/j.epsl.2006.09.018

Li, X.-H., Li, W.-X., Li, Z.-X., Lo, C.-H., Wang, J., Ye, M.-F., & Yang, Y.-H. (2009). Amalgamation between the Yangtze and Cathaysia Blocks in South China: Constraints from SHRIMP U–Pb zircon ages, geochemistry and Nd–Hf isotopes of the Shuangxiwu volcanic rocks. *Precambrian Research*, *174*(1–2), 117–128. https://doi.org/10.1016/j.precamres.2009.07.004

Li, Y., Wang, C., Dai, J., Xu, G., Hou, Y., & Li, X. (2015). Propagation of the deformation and growth of the Tibetan–Himalayan orogen: A review. *Earth-Science Reviews*, *143*, 36–61. https://doi.org/10.1016/j.earscirev.2015.01.001

Liang, S., Gan, W., Shen, C., Xiao, G., Liu, J., Chen, W., et al. (2013). Three-dimensional velocity field of present-day crustal motion of the Tibetan Plateau derived from GPS measurements. *Journal of Geophysical Research: Solid Earth*, *118*, 5722–5732. https://doi.org/10.1002/2013JB010503

Liu, Q. Y., van der Hilst, R. D., Li, Y., Yao, H. J., Chen, J. H., Guo, B., et al. (2014). Eastward expansion of the Tibetan Plateau by crustal flow and strain partitioning across faults. *Nature Geoscience*, *7*(5), 361–365. https://doi.org/10.1038/ngeo2130

Liu, X., & Zhao, D. (2016). Seismic velocity azimuthal anisotropy of the Japan subduction zone: Constraints from P and S wave traveltimes. *Journal of Geophysical Research: Solid Earth*, *121*, 5086–5115. https://doi.org/10.1002/2016JB013116

Long, M. D., & Silver, P. G. (2009). Shear wave splitting and mantle anisotropy: Measurements, interpretations, and new directions. *Surveys in Geophysics*, *30*(4–5), 407–461. https://doi.org/10.1007/s10712-009-9075-1

Molnar, P., & Tapponnier, P. (1975). Cenozoic tectonics of Asia: Effects of a continental collision: Features of recent continental tectonics in Asia can be interpreted as results of the India-Eurasia collision. *Science*, *189*(4201), 419–426. https://doi.org/10.1126/science.189.4201.419

Paige, C. C., & Saunders, M. A. (1982). LSQR: An algorithm for sparse linear equations and sparse least squares. *ACM Transactions on Mathematical Software (TOMS)*, *8*(1), 43–71. https://doi.org/10.1145/355984.355989

Pan, Y., & Shen, W.-B. (2017). Contemporary crustal movement of southeastern Tibet: Constraints from dense GPS measurements. *Scientific Reports*, *7*(1), 45348. https://doi.org/10.1038/srep45348

Pasyanos, M. E., Masters, T. G., Laske, G., & Ma, Z. (2014). LITHO1.0: An updated crust and lithospheric model of the Earth. *Journal of Geophysical Research: Solid Earth*, *119*, 2153–2173. https://doi.org/10.1002/2013JB010626

Plomerová, J., & Babuška, V. (2010). Long memory of mantle lithosphere fabric—European LAB constrained from seismic anisotropy. *Lithos*, *120*(1-2), 131–143. https://doi.org/10.1016/j.lithos.2010.01.008

Raitt, R. W., Shor, G. G., Francis, T. J. G., & Morris, G. B. (1969). Anisotropy of the Pacific upper mantle. *Journal of Geophysical Research*, *74*(12), 3095–3109. https://doi.org/10.1029/JB074i012p03095

Ren, J. (1999). *Tectonic map of China and adjacent regions 1:5 000 000*. Beijing: Geological Pub. House.

Royden, L. H., Burchfiel, B. C., & van der Hilst, R. D. (2008). The geological evolution of the Tibetan Plateau. *Science*, *321*(5892), 1054–1058. https://doi.org/10.1126/science.1155371

Shapiro, N. M., Ritzwoller, M. H., Molnar, P., & Levin, V. (2004). Thinning and flow of Tibetan crust constrained by seismic anisotropy. *Science*, *305*(5681), 233–236. https://doi.org/10.1126/science.1098276

Shearer, P. M. (2009). *Introduction to Seismology*. Cambridge, UK: Cambridge University Press. https://doi.org/10.1017/CBO9780511841552

Shen, W., Ritzwoller, M. H., Kang, D., Kim, Y., Lin, F.-C., Ning, J., et al. (2016). A seismic reference model for the crust and uppermost mantle beneath China from surface wave dispersion. *Geophysical Journal International*, *206*(2), 954–979. https://doi.org/10.1093/gji/ggw175

Shen, Z.-K., Lü, J., Wang, M., & Bürgmann, R. (2005). Contemporary crustal deformation around the southeast borderland of the Tibetan Plateau. *Journal of Geophysical Research*, *110*, B11409. https://doi.org/10.1029/2004JB003421

Shi, Y., Gao, Y., Su, Y., & Wang, Q. (2012). Shear-wave splitting beneath Yunnan area of Southwest China. *Earthquake Science*, *25*(1), 25–34. https://doi.org/10.1007/s11589-012-0828-4

Silver, P. G. (1996). Seismic anisotropy beneath the continents: Probing the depths of geology. *Annual Review of Earth and Planetary Sciences*, *24*(1), 385–432. https://doi.org/10.1146/annurev.earth.24.1.385

Silver, P. G., & Chan, W. W. (1991). Shear wave splitting and subcontinental mantle deformation. *Journal of Geophysical Research*, *96*(B10), 16429–16,454. https://doi.org/10.1029/91JB00899

Sol, S., Meltzer, A., Bürgmann, R., van der Hilst, R. D., King, R., Chen, Z., et al. (2007). Geodynamics of the southeastern Tibetan Plateau from seismic anisotropy and geodesy. *Geology*, *35*(6), 563–566. https://doi.org/10.1130/G23408A.1

Sun, S., Ji, S., Michibayashi, K., & Salisbury, M. (2016). Effects of olivine fabric, melt-rock reaction, and hydration on the seismic properties of peridotites: Insight from the Luobusha ophiolite in the Tibetan Plateau. *Journal of Geophysical Research: Solid Earth*, *121*, 3300–3323. https://doi.org/10.1002/2015JB012579

Sun, Y., Niu, F., Liu, H., Chen, Y., & Liu, J. (2012). Crustal structure and deformation of the SE Tibetan plateau revealed by receiver function data. *Earth and Planetary Science Letters*, *349-350*, 186–197. https://doi.org/10.1016/j.epsl.2012.07.007

Tapponnier, P., Zhiqin, X., Roger, F., Meyer, B., Arnaud, N., Wittlinger, G., & Jingsui, Y. (2001). Oblique stepwise rise and growth of the Tibet Plateau. *Science*, *294*(5547), 1671–1677. https://doi.org/10.1126/science.105978

Toomey, D. R., & Foulger, G. R. (1989). Tomographic inversion of local earthquake data from the Hengill-Grensdalur central volcano complex, Iceland. *Journal of Geophysical Research*, *94*(B12), 17497–17,510. https://doi.org/10.1029/JB094iB12p17497

Um, J., & Thurber, C. (1987). A fast algorithm for two-point seismic ray tracing. *Bulletin of the Seismological Society of America*, *77*(3), 972–986.

Wan, T. (2012). *The tectonics of China: Data, maps and evolution*. Berlin Heidelberg, Berlin: Springer. https://doi.org/10.1007/978-3-642-11868-5

Wang, C.-Y., Flesch, L. M., Silver, P. G., Chang, L.-J., & Chan, W. W. (2008). Evidence for mechanically coupled lithosphere in central Asia and resulting implications. *Geology*, *36*(5), 363–366. https://doi.org/10.1130/G24450A.1

Wang, J., & Zhao, D. (2008). P-wave anisotropic tomography beneath Northeast Japan. *Physics of the Earth and Planetary Interiors*, *170*(1–2), 115–133. https://doi.org/10.1016/j.pepi.2008.07.042

Wang, J., & Zhao, D. (2013). P-wave tomography for 3-D radial and azimuthal anisotropy of Tohoku and Kyushu subduction zones. *Geophysical Journal International*, *193*(3), 1166–1181. https://doi.org/10.1093/gji/ggt086

Wang, S., Jiang, G., Xu, T., Tian, Y., Zheng, D., & Fang, X. (2012). The Jinhe–Qinghe fault—An inactive branch of the Xianshuihe–Xiaojiang fault zone, eastern Tibet. *Tectonophysics*, *544-545*, 93–102. https://doi.org/10.1016/j.tecto.2012.04.004

Wang, W., Wu, J., Fang, L., Lai, G., & Cai, Y. (2017). Crustal thickness and Poisson's ratio in Southwest China based on data from dense seismic arrays. *Journal of Geophysical Research: Solid Earth*, *122*, 7219–7235. https://doi.org/10.1002/2017JB013978

Wei, W., Unsworth, M., Jones, A., Booker, J., Tan, H., Nelson, D., et al. (2001). Detection of widespread fluids in the Tibetan crust by Magnetotelluric studies. *Science*, *292*(5517), 716–719. https://doi.org/10.1126/science.1010580

Wei, W., Zhao, D., & Xu, J. (2013). P-wave anisotropic tomography in Southeast Tibet: New insight into the lower crustal flow and seismotectonics. *Physics of the Earth and Planetary Interiors*, *222*, 47–57. https://doi.org/10.1016/j.pepi.2013.07.002

Weiss, T., Siegesmund, S., Rabbel, W., Bohlen, T., & Pohl, M. (2014). Seismic Velocities and Anisotropy of the Lower Continental Crust: A Review. *Pure and Applied Geophysics*, *156*(1–2), 97–122. https://doi.org/10.1007/s000240050291

Wessel, P., Smith, W. H. F., Scharroo, R., Luis, J., & Wobbe, F. (2013). Generic Mapping Tools: Improved version released. *Eos, Transactions American Geophysical Union*, *94*(45), 409–410. https://doi.org/10.1002/2013EO450001

Xie, J., Ritzwoller, M. H., Shen, W., & Wang, W. (2017). Crustal anisotropy across eastern Tibet and surroundings modeled as a depth-dependent tilted hexagonally symmetric medium. *Geophysical Journal International*, ggx004. https://doi.org/10.1093/gji/ggx004

Xu, Y., Zhong, Y. T., Wei, X., Chen, J., Liu, H. Q., Xie, W., et al. (2017). Permian mantle plume and Earth's surface system evolution. *Bulletin of Mineralogy, Petrology and Geochemistry*, *36*(3), 359–373. https://doi.org/10.3969/j.issn.1007-2802.2017.03.001

Xu, Z., Huang, Z., Wang, L., Xu, M., Ding, Z., Wang, P., et al. (2016). Crustal stress field in Yunnan: Implication for crust-mantle coupling. *Earthquake Science*, *29*(2), 105–115. https://doi.org/10.1007/s11589-016-0146-3

Yao, H., van der Hilst, R. D., & Montagner, J. P. (2010). Heterogeneity and anisotropy of the lithosphere of SE Tibet from surface wave array tomography. *Journal of Geophysical Research*, *115*, B12307. https://doi.org/10.1029/2009JB007142

Yin, A. (2010). Cenozoic tectonic evolution of Asia: A preliminary synthesis. *Tectonophysics*, *488*(1–4), 293–325. https://doi.org/10.1016/j.tecto.2009.06.002

Zhang, P.-Z., Shen, Z., Wang, M., Gan, W., Bürgmann, R., Molnar, P., et al. (2004). Continuous deformation of the Tibetan Plateau from global positioning system data. *Geology*, *32*(9), 809–812. https://doi.org/10.1130/G20554.1

Zhang, Z., Deng, Y., Teng, J., Wang, C., Gao, R., Chen, Y., & Fan, W. (2011). An overview of the crustal structure of the Tibetan plateau after 35 years of deep seismic soundings. *Journal of Asian Earth Sciences*, *40*(4), 977–989. https://doi.org/10.1016/j.jseaes.2010.03.010

Zhao, D., Christensen, D., & Pulpan, H. (1995). Tomographic imaging of the Alaska subduction zone. *Journal of Geophysical Research*, *100*(B4), 6487–6504. https://doi.org/10.1029/95JB00046

Zhao, D., Horiuchi, S., & Hasegawa, A. (1992). Tomographic imaging of P and S wave velocity structure beneath northeastern Japan. *Journal of Geophysical Research*, *97*(B13), 19909–19,928. https://doi.org/10.1029/92JB00603

Zhao, D., Yu, S., & Liu, X. (2016). Seismic anisotropy tomography: New insight into subduction dynamics. *Gondwana Research*, *33*, 24–43. https://doi.org/10.1016/j.gr.2015.05.008

Zhao, J., Yuan, X., Liu, H., Kumar, P., Pei, S., Kind, R., et al. (2010). The boundary between the Indian and Asian tectonic plates below Tibet. *Proceedings of the National Academy of Sciences of the United States of America*, *107*(25), 11229–11233. https://doi.org/10.1073/pnas.1001921107

Zhao, L., Luo, Y., Liu, T. Y., & Luo, Y. J. (2013). Earthquake focal mechanisms in Yunnan and their inference on the regional stress field. *Bulletin of the Seismological Society of America*, *103*(4), 2498–2507. https://doi.org/10.1785/0120120309

Zhao, W., Kumar, P., Mechie, J., Kind, R., Meissner, R., Wu, Z., et al. (2011). Tibetan plate overriding the Asian plate in central and northern Tibet. *Nature Geoscience*, *4*(12), 870–873. https://doi.org/10.1038/ngeo1309

Zheng, G., Wang, H., Wright, T. J., Lou, Y., Zhang, R., Zhang, W., et al. (2017). Crustal deformation in the India-Eurasia collision zone from 25 years of GPS measurements. *Journal of Geophysical Research: Solid Earth*, *122*, 9290–9312. https://doi.org/10.1002/2017JB014465

Zuza, A. V., Cheng, X., & Yin, A. (2016). Testing models of Tibetan Plateau formation with Cenozoic shortening estimates across the Qilian Shan–Nan Shan thrust belt. *Geosphere*, *12*(2), 501–532. https://doi.org/10.1130/GES01254.1